Non-water-stressed canopy temperature for crop water stress index estimation in soybean and maize: growth-stage-specific measurement timing and dynamic modeling

by

Kabateraine Tumwesige

B.S., Makerere University, Kampala, Uganda, 2024

A THESIS

submitted in partial fulfillment of the requirements for the degree

MASTER OF SCIENCE

Carl and Melinda Helwig Department of Biological and Agricultural Engineering
Carl R. Ice College of Engineering

KANSAS STATE UNIVERSITY
Manhattan, Kansas

2026

Approved by:

Major Professor
Dr. Daran R. Rudnick

Copyright

© Kabateraine Tumwesige 2026.

Abstract

Efficient irrigation management in water-limited cropping systems depends on timely identification of crop water stress, yet thermal methods remain limited by the difficulty of establishing a representative non-water-stressed canopy-temperature reference. This thesis evaluated two complementary, growth-stage-aware approaches for strengthening that reference: selecting appropriate measurement times for soybean non-water-stressed baselines and dynamically predicting non-water-stressed canopy temperature in maize. Canopy-temperature and meteorological observations were collected during the 2018 to 2020 growing seasons at North Platte, Nebraska. For soybean, candidate measurement periods were compared within a Bayesian hierarchical framework using the relationship between the resulting crop water stress index estimates and yield. For maize, an energy-balance-informed, data-based mechanistic model represented non-water-stressed canopy temperature as a first-order continuous-time system driven by air temperature, solar radiation, and vapor pressure deficit. The selected soybean periods shifted from mid-to-late afternoon during vegetative development to midday or early afternoon during reproductive development. Relative to these selected periods, the conventional period from 2:00 to 3:00 p.m. increased posterior mean root mean square error by 3.3 to 43.0 percent. Baseline slopes and intercepts also varied among growth stages. In maize, model performance was strongest at the milk and dough stages, where mean absolute error ranged from 0.093 to 0.342 degrees Celsius and the coefficient of determination reached 0.958; performance was weaker at the V8, V9, and blister stages. Collectively, the results show that the non-water-stressed thermal reference changes with crop development. Accounting for growth stage in both measurement timing and dynamic prediction can improve the consistency of crop water stress index estimation and strengthen its use in irrigation management.

Table of Contents

List of Figures vi
List of Tables viii
Acknowledgements ix
Dedication xi
Preface xii
Chapter 1 - General Introduction 1
1.1. Problem Statement 1
1.2. Statement of Objectives 4
Chapter 2 - Identification of Growth-Stage-Specific Best Time-of-Day Windows for Developing Non-Water-Stressed Baselines to Estimate Soybean Crop Water Stress Index 5
Abstract 5
2.1. Introduction 7
2.2. Materials and Methods 12
2.2.1. Site Description 12
2.2.2. Data Collection 15
2.2.3. Data Analysis 16
2.2.3.1. Non-Water-Stressed Canopy Temperature and Dynamic Baseline Development 17
2.2.3.2. Best TOD Measurement Period Identification Using Bayesian Modeling 19
2.3. Results 23
2.3.1. Irrigation Effects on Soybean Yield 23
2.3.2. Best Time-of-Day Measurement Period for NWSB Development 24
2.3.3. Growth-Stage-Specific NWSBs at the Best Time-of-Day Measurement Periods 29
2.4. Discussion 31
2.5. Conclusions 35
Chapter 3 - Dynamic Data-Based Mechanistic Modeling of Non-Water-Stressed Maize Canopy Temperature for Crop Water Stress Index Estimation 37
Abstract 37

3.1. Introduction 38
3.2. Materials and Methods 42
3.2.1. Site Description and Experimental Design 42
3.2.2. Instrumentation and Data Collection 44
3.2.3. Mechanistic Model Formulation 46
3.2.4. Data-Based Mechanistic Modeling Approach, Implementation, and Parameter Estimation 49
3.3. Results and Discussion 53
3.3.1. Cross-Year Predictive Performance of the DBM Model 53
3.3.2. Error Structure and Stage-Specific Model Behavior 57
3.3.3. Implications for Empirical CWSI Estimation and Irrigation Water Management 60
3.4. Conclusions 62
Chapter 4 - Summary and Conclusions 64
4.1. Conclusions 64
4.2. Future Work 65
References 66
Appendix A - Growth-Stage-Specific Model Parameter Estimates and Advective Delays 76

List of Figures

Figure 2.1. Measurement-period-specific RMSE posterior distribution profiles used to identify the best time-of-day (TOD) measurement period for NWSB performance during the late vegetative stages (V5, V6, and V7) and the early reproductive stage (R1). The black line shows the estimated RMSE for each 15-min time-of-day period, and the shaded purple band represents the 90% credible interval from the Bayesian analysis. The red arrow indicates the selected best measurement period, and the inset box reports the posterior probability..... 26

Figure 2.2. Time-period-specific posterior RMSE profiles for identifying the best TOD measurement period for NWSB development during reproductive stages R2–R6. The black line represents posterior mean RMSE, the shaded band indicates the 90% credible interval, and the red arrow marks the selected best TOD measurement period with its posterior probability shown in the inset. 27

Figure 2.3. Growth-stage-specific NWSBs relating soybean $Tc - Ta$ to VPD, developed after identifying the best time-of-day (TOD) measurement period for each growth stage. Vegetative-stage baselines (V5–V7) used the available observations from 2019 and 2020, whereas reproductive-stage baselines (R1–R6) used observations from 2018–2020. Each panel corresponds to one soybean growth stage (V5 to R6) and its selected best TOD period. Blue points represent the available pooled Tc − Ta and VPD observations from the three years, red lines show the fitted stage-specific linear NWSBs, and the displayed equations are the resulting pooled baseline relationships. 31

Figure 3.1. Data-based mechanistic modeling framework used for identification and evaluation of the maize canopy temperature model. Input data (Tc, Ta, Rs, and VPD) were filtered to the 12:30–16:30 period, stratified by growth stage, and aggregated into minute-of-day averages before model training and independent cross-year testing. During training, input delays and model parameters were identified for the first-order dynamic canopy temperature model, and predictive performance on the test year was assessed using $R2$, MAE, and RMSE. 52

Figure 3.2. Stage-specific cross-year predictive performance of the DBM canopy temperature (Tc) model. In each panel, observed and modeled Tc are compared using time-series plots and observed-versus-modeled scatter plots. Panel A corresponds to training on 2019 and testing on 2018, Panel B to training on 2019 and testing on 2020, Panel C to training on 2020 and

testing on 2019, Panel D to training on 2018 and testing on 2020, and Panel E to training on 2020 and testing on 2018. The accompanying $R2$ and MAE statistics quantify goodness-of-fit and prediction error, respectively, for each maize growth stage under independent validation. Here, $VTR1$ denotes the combined tasseling-to-silking stage. 57
Figure 3.3. Distribution of model prediction errors across maize growth stages (V8–R4). Violin plots represent the density of errors for each stage, with overlaid points showing individual observations. The white markers indicate mean prediction error, and the horizontal bars represent variability around the mean. The dashed horizontal line at zero denotes perfect model agreement, where positive values indicate underestimation and negative values indicate overestimation by the model. 59

List of Tables

Table 2.1. Mean (± standard deviation) physical, organic matter content (OMC), and hydraulic characteristics throughout the 3.0 m soil profile from 72 sampling points across the study area. 13

Table 2.2. Monthly mean weather conditions during the experimental growing seasons (2018–2020) and an 18-year seasonal weather (2000–2017), including daily minimum air temperature (T_{min}), maximum air temperature (T_{max}), average relative humidity (RH_{avg}), wind speed at 3 m height (U_3), incoming solar radiation (R_s), cumulative precipitation (P), and grass-based reference evapotranspiration (ET_o). 15

Table 2.3. Seasonal total irrigation amount (I, mm) and soybean yield (Mg ha^{-1}) for FIT, 60% FIT, and rainfed treatments in 2018, 2019, and 2020. Yield values are mean ± standard error. Different letters within a year indicate significant differences among treatments at $P < 0.05$. 24

Table 2.4. Posterior mean RMSE of the CWSI–yield relationship for the selected growth-stage-specific best TOD periods and the conventional fixed 14:00–15:00 h period in soybean. Conventional penalty represents the percentage increase in RMSE relative to the selected best TOD period. 28

Table 3.1. Mean (± standard error) minimum air temperature (T_{min}), maximum air temperature (T_{max}), and incoming solar radiation (R_s) during daytime measurement periods across maize phenological growth stages for the 2018, 2019, and 2020 growing seasons. 45

Table 3.2. Interannual dynamic transferability performance of the DBM model for predicting Tc, ns across maize growth stages, expressed as $R2$, MAE (°C), and RMSE (°C). 54

Table A.1. Growth-stage-specific parameter estimates of the DBM model under cross-year calibration and validation for maize Tc, ns. Values of a, b, and c are reported with approximate standard errors in parentheses. 76

Table A.2. Stage-specific delay combinations selected for DBM model identification under different training and testing year combinations. The delays τa, τb, and τc represent the selected integer-minute lags for air temperature, Rs, and vapor pressure deficit, respectively. 77

Acknowledgements

Above all, I thank Almighty God for His grace and guidance throughout my life, especially during this journey. In moments of challenge, uncertainty, and frustration, He remained my constant source of wisdom and hope. Without His sustaining grace, this accomplishment would not have been possible.

I am profoundly grateful to my major advisor, Dr. Daran R. Rudnick, for recognizing my potential and offering me an internship opportunity in 2024 and, subsequently, the opportunity to return as a graduate research assistant in June 2025. These opportunities have changed the course of my life. His guidance, patience, encouragement, and willingness to explain concepts repeatedly have greatly strengthened my confidence and competence as a student. I will remain forever grateful for his mentorship and the confidence he placed in me.

I sincerely thank Dr. Josefina Lacasa for generously sharing her knowledge and dedicating time to our weekly meetings. Her patience and guidance were instrumental in completing this work and strengthening my understanding, especially in statistics. I also thank Dr. Trevor Hefley for his valuable statistical insights and Dr. Chris Proctor for serving on my graduate committee and continually supporting encouraging my professional growth.

My heartfelt appreciation goes to the K-State Testing Ag Performance Solutions team, particularly Raenette Martin, Ray Duffey, Kelsey Stremel, and Renne Jones, for their professional and personal support. I especially thank my lab mate, Rayhaan Kabenge, for always being available to discuss ideas and help. I also appreciate my fellow graduate students and the faculty and staff of the department for their encouragement and friendship.

I remain grateful to Dr. Isa Kabenge and Dr. Allan John Komakech for their guidance and contributions to the academic foundation that prepared me for graduate study. I similarly thank Dr.

Abia Katimbo, Dr. Hope Nakabuye, and Martha Nabaggala for supporting me before and after my transition from Uganda to the United States.

I thank the St. Isidore's Catholic Student Center community for becoming my spiritual home and a place of peace, prayer, friendship, and belonging. I am equally grateful to the Crossroads community and the friends I met there for their kindness and companionship.

Finally, I offer my deepest gratitude to my mother, Mary Kobusinge; my father, Stephen Kabateraine; my brother, Mugisa Kabateraine; and my sisters, Businge Kabateraine, Atuhaire Kabateraine, and Tushemerirwe Unity, for their unwavering love, prayers, encouragement, and belief in me. My mother's perseverance and sacrifices have continually inspired me to give my best and become a better version of myself.

I am also deeply grateful to Mr. and Mrs. Kalyango and their children, whose friendship, encouragement, calls, and regular check-ins gave me strength and reminded me that I was never alone. To everyone who contributed to this journey, I offer my sincere and heartfelt gratitude.

Dedication

This thesis is dedicated to everyone committed to improving water-use irrigation efficiency and developing sustainable solutions for agriculture in water-scarce regions, particularly communities dependent on the High Plains Aquifer. I hope this work contributes, even in a small way, to preserving limited water resources while sustaining agricultural livelihoods.

Most especially, I dedicate this work to my mother, Mary Kobusinge. Growing up on our crop-and-livestock farm, I watched her wait and pray for rain because the well-being of our crops, animals, and family depended on it. Her perseverance through that uncertainty helped shape my desire to contribute to more reliable and sustainable irrigation. As this research advances that effort, I hope she sees in it the purpose that grew from those experiences and, above all, I hope it makes her proud.

Preface

This thesis brings together two related studies developed to address a practical limitation in canopy-temperature-based crop water stress assessment: the need for a reliable non-water-stressed reference. Chapter 2 investigates the selection of growth-stage-specific time-of-day periods for developing non-water-stressed baselines in soybean, while Chapter 3 develops a dynamic data-based mechanistic framework for predicting non-water-stressed canopy temperature in maize. Together, the two studies examine complementary approaches for improving the estimation of the crop water stress index under field conditions.

At the time of completing this thesis, Chapter 2 had been submitted to a peer-reviewed journal and was under review, while Chapter 3 was being prepared for submission to a peer-reviewed journal.

Chapter 1 - General Introduction

1.1. Problem Statement

Efficient irrigation management in semi-arid cropping systems requires timely and reliable information about crop water status. This is especially important where producers must sustain crop productivity while conserving limited water supplies. Canopy temperature provides a plant-based indicator of water stress because it reflects the balance between absorbed energy and heat dissipated through transpiration. Under non-water-stressed conditions, transpiration promotes evaporative cooling and generally maintains the canopy near or below air temperature. When water becomes limiting, stomatal closure reduces transpiration and canopy temperature increases (Jackson, 1982; Jones, 1999). This physiological response provides the basis for the crop water stress index (CWSI), which expresses the thermal conditions of a crop relative to non-water-stressed and fully stressed reference conditions (Idso et al., 1981; Jackson et al., 1981).

Although the empirical CWSI is attractive for irrigation management because it uses canopy temperature and commonly measured weather variables, its accuracy depends on the thermal references used in its calculation. The non-water-stressed reference, commonly expressed as a non-water-stressed baseline (NWSB) or the corresponding non-water-stressed canopy temperature ($T_{c,ns}$), defines the expected thermal behavior of a fully transpiring crop under the prevailing environment. Because every observed canopy temperature is interpreted relative to this reference, an unrepresentative NWSB or $T_{c,ns}$ can cause crop water stress to be overestimated or underestimated and can weaken the relationship between CWSI and agronomic responses such as yield.

A central difficulty is that the non-water-stressed reference is not a fixed crop characteristic. It is influenced by solar radiation, air temperature, vapor pressure deficit (VPD),

wind, and the exchange of sensible and latent heat between the canopy and atmosphere. It also changes as leaf area, canopy height, architecture, stomatal behavior, and aerodynamic resistance evolve during crop development. Consequently, the canopy-temperature response of a well-watered crop may vary within a day, among growth stages, and across growing seasons (Han et al., 2018; Liao et al., 2024; Payero et al., 2005a; Wanjura et al., 1990). A reference developed without accounting for these sources of variation may therefore be valid only for the environmental and developmental conditions under which it was established.

This variability creates uncertainty about which canopy-temperature observations should be used for NWSB development. Previous studies have used measurement periods ranging from narrow intervals near midday to broader periods extending through the afternoon. These periods have often been selected from convention, anticipated high atmospheric demand, or previous studies rather than through systematic evaluation of the resulting CWSI performance (Irmak et al., 2000; Katimbo et al., 2022; Nielsen, 1994). Moreover, applying one fixed measurement period throughout the season assumes that the most representative observation period remains unchanged as the crop develops. Changes in canopy structure, transpiration, and crop–atmosphere coupling make this assumption uncertain. Thus, a defensible procedure is needed for selecting measurement periods that reflect crop developmental differences and produce baselines with a meaningful relationship to crop response.

An additional limitation is the dependence of empirical CWSI on direct measurements from a fully irrigated reference crop. Maintaining such a reference throughout the growing season may require dedicated land, additional water, separate sensors, and continuous management to ensure that the crop remains non-water stressed. These requirements can be accommodated in research experiments but reduce the practicality of routine CWSI application in producers' fields.

Wet and dry artificial reference surfaces have been proposed as substitutes, but differences between these materials and actual crop leaves in emissivity, geometry, heat capacity, and aerodynamic properties may prevent them from reproducing the canopy energy balance accurately (Jones, 2004; Jones et al., 2002; Maes & Steppe, 2012). The availability of a representative non-water-stressed reference therefore remains an important barrier to operational and automated canopy-temperature-based irrigation management.

Weather-based prediction offers a potential means of estimating $T_{c,ns}$ without continuously maintaining a well-watered reference. Regression and machine-learning approaches have demonstrated that non-water-stressed canopy or leaf temperature can be estimated from meteorological variables (King & Shellie, 2016; Nakabuye et al., 2022; Payero et al., 2005a). However, most existing approaches represent canopy temperature as a static or contemporaneous function of weather conditions. Canopy temperature may respond to changes in solar radiation, air temperature, and VPD at different rates and after different delays because of thermal storage, stomatal adjustment, plant hydraulic processes, and canopy–atmosphere coupling (Al-Faraj et al., 2000; Schymanski et al., 2013). Dynamic data-based mechanistic modeling can represent these time-dependent responses by combining physical understanding with data-based estimation of system parameters and input-specific delays (Taylor et al., 2007; Young, 2006). Although this approach has been used to estimate CWSI baseline temperatures under greenhouse conditions (Adeyemi et al., 2018), its ability to predict $T_{c,ns}$ for field-grown crops under variable semi-arid conditions and across crop growth stages and growing seasons remains insufficiently established.

The overarching problem is therefore the absence of a sufficiently reliable and operational framework for characterizing the non-water-stressed thermal reference under changing environmental and crop-development conditions. Measurement timing, growth-stage variability,

dependence on well-watered reference treatments, and the delayed thermal response of the canopy are interrelated aspects of this broader problem. Addressing them requires complementary approaches that improve both the selection of observations used to establish the reference and the prediction of reference temperature from routinely measured meteorological variables. Such advances are needed to strengthen the consistency, interpretation, and practical application of CWSI for irrigation management in water-limited cropping systems.

1.2. Statement of Objectives

The overall goal of this thesis was to improve the reliability and operational applicability of empirical CWSI estimation by strengthening the characterization and prediction of the non-water-stressed canopy-temperature reference under changing environmental and crop-development conditions. The specific objectives were to (1) identify suitable growth-stage-specific time-of-day measurement periods for developing soybean NWSBs by evaluating the relationship between the resulting CWSI estimates and yield while accounting for interannual variability, and then develop NWSBs using the selected periods; and (2) develop an energy-balance-informed, data-based mechanistic model for predicting non-water-stressed maize canopy temperature from air temperature, solar radiation, and VPD, and evaluate its predictive performance across independent growing seasons and maize growth stages.

Chapter 2 - Identification of Growth-Stage-Specific Best Time-of-Day Windows for Developing Non-Water-Stressed Baselines to Estimate Soybean Crop Water Stress Index

Abstract

Accurate estimation of the crop water stress index (CWSI) depends on a representative non-water-stressed baseline (NWSB), yet the most suitable time-of-day (TOD) period for collecting canopy-temperature (T_c) and meteorological observations remains inconsistently defined. This study identified growth-stage-specific TOD periods for soybean NWSB development using field observations collected during 2018–2020 at North Platte, Nebraska, USA, under full irrigation, 60% of full irrigation, and rainfed treatments. Candidate 15-min periods between 12:00 and 17:00 h were evaluated with a moving-window framework, and performance was assessed using root mean square error (RMSE) from the relationship between CWSI and yield. A Bayesian hierarchical model accounted for interannual variability. Selected periods occurred in the mid-to-late afternoon during vegetative stages (15:15–15:30 at V5, 14:45–15:00 at V6, and 14:00–14:15 at V7) and closer to solar noon or early afternoon during reproductive stages (12:30–12:45 at R1, 12:00–12:15 at R2, 12:15–12:30 at R3, 13:00–13:15 at R4, 12:00–12:15 at R5, and 13:00–13:15 at R6). The conventional 14:00–15:00 h period produced posterior mean RMSE values 3.3–43.0% higher than those obtained using the selected periods. The resulting NWSBs had negative slopes, and both slopes and intercepts differed among growth stages. These findings indicate that soybean NWSB development should account for growth stage rather than rely on one fixed seasonal measurement period.

Keywords: canopy temperature; canopy-to-air temperature difference; Bayesian hierarchical modeling; infrared thermometry; irrigation water management; thermal sensing; crop water stress assessment.

2.1. Introduction

Canopy temperature (T_c)-based approaches have long been used as a practical means of assessing crop water status for irrigation water management (Baker et al., 2013; Bockhold et al., 2011; Clawson et al., 1989; Geiser et al., 1982; Wanjura et al., 2003). The foundational framework for interpreting T_c as a quantitative indicator of plant water stress was established by Idso et al. (1981), who proposed an empirical formulation of the crop water stress index (CWSI), and by Jackson et al. (1981), who developed a theoretical energy-based formulation. Both contributions enabled the operational use of T_c measurements in irrigation scheduling. The underlying basis for this relationship lies in plant physiological and energy balance processes. Under well-watered (i.e., non-water-stressed) conditions, crop transpiration induces evaporative cooling, keeping T_c lower than or close to air temperature (T_a). In contrast, water stress reduces stomatal conductance and transpiration, limiting evaporative cooling and causing T_c to rise (Sapkota et al., 2023). By normalizing this thermal response relative to non-water-stressed and fully stressed reference conditions, CWSI provides a dimensionless, physically interpretable measure of plant water status (Idso et al., 1981).

The empirical formulation of CWSI as described by Idso et al. (1981) is expressed as:

$$CWSI = \frac{(T_c - T_a) - (T_c - T_a)_{LB}}{(T_c - T_a)_{UB} - (T_c - T_a)_{LB}} \quad (2.1)$$

where $(T_c - T_a)$ is the observed canopy-to-air temperature difference, $(T_c - T_a)_{LB}$ is the non-water-stressed baseline (NWSB), commonly referred to as the lower baseline (LB), representing the lower limit, and $(T_c - T_a)_{UB}$ is the upper baseline (UB) corresponding to non-transpiring (fully stressed) conditions. By scaling T_c between these two limits, CWSI yields a dimensionless index ranging from 0 to 1, where values near 0 represent a fully transpiring, non-water-stressed crop, and values approaching 1 indicate a non-transpiring, severely water-stressed crop. This normalized

framework has made CWSI particularly useful in irrigation water management, where threshold values for specific crops have been used to guide irrigation timing and scheduling under field conditions (Fattahi et al., 2018; Osroosh et al., 2015; Yuan et al., 2004).

Theoretical and empirical approaches have been developed to estimate CWSI for irrigation water management. The theoretical formulation, based on canopy energy balance principles (Jackson, 1982), incorporates net radiation and crop resistance parameters, including aerodynamic and surface resistance. While this approach provides a physically rigorous description of T_c dynamics, its practical implementation is constrained by the difficulty of accurately measuring or estimating resistance terms under field conditions. Aerodynamic and surface resistances are not directly measurable and are typically inferred using simplified parameterizations, introducing uncertainty into model outputs (Allen et al., 1998; Campbell & Norman, 2000). Furthermore, the requirement for continuous measurement of energy balance components, such as net radiation and heat fluxes, requires specialized instrumentation that is not readily available in operational agricultural settings, thereby increasing its operational complexity under field conditions (Payero et al., 2005a).

In contrast, the empirical approach relies on readily measurable variables, specifically the canopy-to-air temperature difference ($T_c - T_a$) and vapor pressure deficit (VPD), making it more suitable for practical application. Its simplicity and operational feasibility have facilitated its widespread adoption in irrigation scheduling and crop water stress monitoring, particularly where locally calibrated baselines are available (Fattahi et al., 2018; Testi et al., 2008; Yazar et al., 1999). However, because empirical CWSI calculation relies on the NWSB and the UB, as described in Equation 2.1, accurate and consistent characterization of these baselines is essential for reliable CWSI estimates. Although both baselines contribute to CWSI, the UB has often been represented

in empirical applications as a fixed value corresponding to a non-transpiring canopy (Irmak et al., 2000; Nakabuye et al., 2022; Shae et al., 1999; Steele et al., 1994; Taghvaeian, Comas, et al., 2014). In contrast, the NWSB has been extensively studied and modeled from the relationship between $(T_c - T_a)$ and VPD under non-stressed conditions.

Empirically, the NWSB is typically determined from diurnal and concurrent measurements of $(T_c - T_a)$ and VPD under well-watered conditions. Despite its widespread use, the best time of day (TOD) for collecting measurements used to develop the NWSB has not been consistently defined. Gardner et al. (1992) recommended collecting measurements of $(T_c - T_a)$ and VPD throughout an entire growing season at the TOD that water stress measurements are most likely to be made (typically early noon to midafternoon). Wanjura et al. (1990) demonstrated that omitting early morning readings from the diurnal datasets improved the coefficient of determination of linear regressions fitted to the data and enhanced the seasonal stability of NWSB slopes. These studies suggest that measurement timing is important, yet they do not establish a single standardized TOD measurement period nor provide a systematic procedure for selecting the best TOD measurement period for NWSB development.

The wide variation in TOD measurement periods used across CWSI studies is evident in the literature. For instance, Irmak et al. (2000) used observations collected between 12:00 and 13:00 h, Nielsen (1994) used observations from 13:15 to 14:00 h, Katimbo et al. (2022) used measurements collected between 12:00 and 16:00 h, Yazar et al. (1999) used measurements obtained between 13:00 and 15:00 h, and Alderfasi and Nielsen (2001) used measurements obtained between 10:00 and 16:00 h. These differences may reflect, in part, the sensitivity of $(T_c - T_a)$ to meteorological conditions such as available energy and wind speed, which differ across locations, seasons, and measurement periods (Payero et al., 2005a). Therefore, NWSBs developed

from different TOD measurement periods may differ for the same crop even within the same climatic region. For example, maize studies conducted in similar regions but across different locations and years have reported differing NWSBs (DeJonge et al., 2015; Han et al., 2018; Idso, 1982; Katimbo et al., 2022; Steele et al., 1994; Taghvaeian, Chávez, et al., 2014). Similarly, Abdul-Jabbar et al. (1985), Hattendorf et al. (1988) and Grimes et al. (1992) reported differing NWSBs for alfalfa under arid and semiarid conditions in the United States. For soybean, Candogan et al. (2013), Morales-Santos and Nolz (2023), and Nielsen (1990) reported distinct NWSBs for soybean in studies conducted in Turkey, Austria, and the United States, respectively. Although these differences may be environmentally justified, they complicate direct comparison among studies and highlight the need for a systematic approach to identify the most suitable TOD period for NWSB development.

Beyond the TOD measurement period, NWSBs have been shown to vary with crop growth stage, further complicating the standardization of CWSI. For example, Wanjura et al. (1990) reported that the slope of the NWSB for cotton became increasingly negative with plant development until canopy cover reached approximately 70%. Han et al. (2018) noted that CWSI may fail to adequately capture irrigation responses or differentiate crop water stress at critical growth stages, partly because aerodynamic resistance varies throughout crop development. Although aerodynamic resistance is not explicitly included in the empirical CWSI formulation, its influence is implicitly reflected in the measured $(T_c - T_a)$. Aerodynamic resistance regulates sensible heat exchange between the canopy and the atmosphere (Javadian et al., 2024; Monje & Bugbee, 2019).

This growth-stage dependency is physically justified: as crops develop, changes in canopy structure, leaf area index (LAI), and canopy height alter the partitioning of available energy

between latent and sensible heat fluxes (Allen et al., 1998; Monteith & Unsworth, 2013). As LAI increases, a greater proportion of net radiation is dissipated as latent heat flux due to enhanced transpiration, while sensible heat flux decreases, thereby influencing T_c and its relationship with atmospheric demand (Campbell & Norman, 2000; Norman et al., 1995). Changes in aerodynamic resistance and canopy coupling to the atmosphere during crop development further modify canopy–air temperature gradients (Hatfield & Prueger, 2015). Therefore, the TOD at which the $(T_c - T_a)$–VPD relationship is most diagnostic of water status is expected to shift across growth stages, meaning that a single fixed TOD measurement period may not be appropriate throughout the growing season. Among widely cultivated irrigated crops, soybean (*Glycine max* L.) has been recognized as particularly sensitive to water deficit during critical developmental stages, making accurate detection of crop water stress essential for maintaining yield stability and water use efficiency (Candogan et al., 2013; Nielsen, 1990). Given that both diurnal environmental dynamics and crop developmental changes influence T_c response, the use of a single fixed TOD measurement period for NWSB development may result in inconsistent or suboptimal characterization of crop water status across the growing season.

Despite the widespread use of CWSI as an indicator of crop water status, clear guidance on the best TOD measurement period for NWSB development for computing CWSI has remained limited, particularly in a growth-stage-specific context. The existing literature reveals substantial variation in TOD measurement periods used across studies, with measurement windows spanning up to six hours, and different NWSBs reported, even for the same crop and climatic region. Most previous studies have selected and used a predefined TOD measurement period based on established conventions, expected high atmospheric demand, or prior literature. However, the best TOD measurement period for NWSB development has not been clearly identified across soybean

growth stages. Therefore, the overall goal of this study was to improve the reliability of empirical CWSI estimation by determining the most suitable TOD measurement periods for NWSB development across soybean growth stages. Specifically, the objectives were to (1) identify the best TOD measurement period for developing the non-water-stressed baseline (NWSB) for CWSI estimation for various growth stages of soybean (*Glycine max* L.), and (2) develop the NWSBs for soybeans at the identified best TOD measurement periods.

2.2. Materials and Methods

2.2.1. Site Description

The study was conducted during the 2018, 2019, and 2020 growing seasons at the University of Nebraska–Lincoln West Central Research, Extension, and Education Center (WCREEC) in North Platte, Nebraska, USA (41.1°N, 100.8°W; elevation 861 m above sea level). The predominant soil type at the site is Cozad silt loam. To characterize the physical properties of the site, soil samples were collected from 72 sampling locations across the field in increments of 0.3 m up to a depth of 3 m as first presented by Nakabuye et al. (2022). The samples were analyzed for sand, silt, and clay by a commercial laboratory (Ward Laboratories, Kearney, NE, USA), and the resulting physical and hydraulic properties of the study area are presented in Table 2.1. Across the 3.0 m profile, sand, clay, and silt contents ranged from 33.3 to 50.7%, 17.1 to 23.5%, and 31.3 to 43.3%, respectively; organic matter content ranged from 0.80 to 2.0%. The procedures of Saxton and Rawls (2006) were adopted to estimate the field capacity (FC) and wilting point (WP) of the soil. As shown in Table 2.1, the FC and WP values across the 3.0 m soil profile ranged between 0.22–0.30 $m^3\ m^{-3}$ and 0.10–0.15 $m^3\ m^{-3}$, respectively.

Table 2.1. Mean (± standard deviation) physical, organic matter content (OMC), and hydraulic characteristics throughout the 3.0 m soil profile from 72 sampling points across the study area.

Soil depth (m)	Sand (%)	Clay (%)	Silt (%)	OMC (%)	Field capacity ($m^3\ m^{-3}$)	Wilting point ($m^3\ m^{-3}$)
0.00–0.30	47.7 ± 5.7	19.0 ± 2.8	33.3 ± 5.8	2.0 ± 0.3	0.25 ± 0.02	0.13 ± 0.02
0.30–0.61	45.3 ± 5.5	20.9 ± 4.9	33.8 ± 4.0	1.5 ± 0.2	0.26 ± 0.03	0.14 ± 0.03
0.61–0.91	45.0 ± 9.7	22.6 ± 6.7	32.4 ± 8.3	1.7 ± 0.3	0.27 ± 0.05	0.15 ± 0.04
0.91–1.22	33.3 ± 5.2	23.5 ± 3.0	43.3 ± 3.8	1.6 ± 0.4	0.30 ± 0.02	0.15 ± 0.02
1.22–1.52	50.7 ± 4.7	15.5 ± 2.2	33.8 ± 4.5	1.0 ± 0.2	0.22 ± 0.02	0.10 ± 0.01
1.52–1.83	46.9 ± 5.7	18.2 ± 4.2	34.9 ± 4.0	1.0 ± 0.2	0.24 ± 0.03	0.12 ± 0.03
1.83–2.13	49.6 ± 6.0	19.1 ± 4.3	31.3 ± 7.5	1.1 ± 0.2	0.24 ± 0.03	0.12 ± 0.03
2.13–2.44	46.9 ± 5.1	17.1 ± 2.3	36.1 ± 4.0	1.1 ± 0.2	0.24 ± 0.02	0.11 ± 0.01
2.44–2.74	46.4 ± 4.9	17.8 ± 2.4	35.8 ± 3.6	0.8 ± 0.1	0.24 ± 0.02	0.11 ± 0.01
2.74–3.05	49.0 ± 4.2	14.9 ± 2.5	36.1 ± 4.2	0.8 ± 0.1	0.22 ± 0.02	0.10 ± 0.02

The experiment consisted of three irrigation treatments: (i) full irrigation (FIT), which received 100% of crop water requirements; (ii) deficit irrigation (60% FIT), which received 60% of full irrigation to induce water stress; and (iii) rainfed, which received no irrigation throughout the growing seasons. The study was arranged in a three-block randomized complete block design (RCBD), with individual plot dimensions of 9.1 m × 72.2 m. Soil water content was monitored using field-calibrated CPN 503 Elite Hydroprobe and CPN 503DR (InstroTek, CA, USA) neutron moisture meter (NMM). These measurements were used to compute maximum allowable depletion (MAD), and irrigation in the FIT treatment was triggered when soil water depletion reached 50% of MAD. Total irrigation applied in the FIT treatment was 173, 61, and 241 mm in 2018, 2019, and 2020, respectively. Correspondingly, the 60% FIT treatment received 104, 37, and 145 mm of irrigation in those respective years. A subsurface drip irrigation system was used to supply irrigation. Driplines were spaced 1.52 m apart and installed at a depth of 0.40 m.

Soybean (*Glycine max L.*) was grown under consistent agronomic management. All cultivars were planted in a north–south orientation at a seeding rate of 474,442 seeds ha^{-1} in 0.76 m rows at a depth of 32 mm using a precision planter. Cultivar and planting date varied by year: Pioneer P24T19R was planted on May 8, 2018; Pioneer P24A99X on May 17, 2019; and Pioneer P23A32X on April 29, 2020. Although cultivar selection differed among years due to seed availability, all varieties were locally adapted and represented comparable maturity groups to maintain interannual consistency. Pest and weed management practices, including herbicide applications, were implemented uniformly across treatments to minimize biotic stress and prevent confounding effects. Harvest occurred on September 28, 2018; September 30, 2019; and October 2, 2020, using a field-calibrated John Deere 9500 combine, and grain yield was determined from the center eight rows of each 12-row plot to minimize border effects.

Weather data for the study site were obtained from an automatic weather station (North Platte 3SW Beta), located 100 m away from the experimental field, operated as part of the Nebraska Mesonet. Weather variables were recorded at 1-minute intervals and included minimum and maximum air temperature (T_a), incoming shortwave solar radiation (R_s), wind speed at 3 m height (U_3), precipitation (P), and relative humidity (RH). Monthly mean grass-based reference evapotranspiration (ET_o) was computed based on the procedures described by Allen et al. (2005). To characterize each experimental growing season as relatively dry or wet, historical weather data from 2000 to 2017 were averaged and summarized alongside the experimental season data in Table 2.2. During the May-to-September period, mean R_s was 20.26, 20.18, and 21.62 MJ m^{-2} d^{-1} in 2018, 2019, and 2020, respectively, compared with the long-term average of 21.08 MJ m^{-2} d^{-1}. Corresponding mean monthly ET_o values were 148, 136, and 168 mm, respectively, relative to a long-term average of 154 mm. Mean monthly precipitation was 83, 108, and 45 mm, respectively,

compared with the long-term monthly average of 63 mm. Thus, 2020 experienced below-normal rainfall with higher ET_o demand, whereas 2019 was wetter with lower ET_o, and 2018 was close to normal conditions.

Table 2.2. Monthly mean weather conditions during the experimental growing seasons (2018–2020) and the 18-year seasonal mean (2000–2017), including daily minimum air temperature (T_{min}), maximum air temperature (T_{max}), average relative humidity (RH_{avg}), wind speed at 3 m height (U_3), incoming solar radiation (R_s), cumulative precipitation (P), and grass-based reference evapotranspiration (ET_o).

Year	Month	T_{min}	T_{max}	RH_{avg}	U_3	P	R_s	ET_o
		(°C)	(°C)	(%)	(m s^{-1})	(mm)	(MJ m^{-2} d^{-1})	(mm)
2018	May	10.3	24.1	67.3	2.6	147.1	19.4	141.9
	June	15.5	28.9	67.8	3.3	102.5	24.4	178.3
	July	16.9	29.2	72.1	2.5	97.4	24.0	168.5
	August	15.0	28.3	70.0	2.2	25.9	19.0	137.1
	September	10.0	25.0	68.8	2.9	41.1	14.5	116.2
2019	May	5.2	17.8	71.5	2.9	163.0	17.4	104.6
	June	12.3	26.4	67.5	2.4	81.5	23.6	154.8
	July	17.8	29.5	70.3	2.3	174.7	24.2	168.6
	August	16.2	27.0	78.0	2.0	93.5	18.0	119.5
	September	12.7	27.7	66.9	2.9	25.9	17.7	133.2
2020	May	7.0	19.9	68.7	2.8	82.5	20.7	124.8
	June	15.3	31.3	57.6	3.6	12.4	24.8	212.3
	July	17.4	31.0	67.4	2.9	111.5	23.6	186.5
	August	15.8	31.0	63.7	2.8	4.8	22.0	177.6
	September	8.9	25.7	58.6	2.8	15.2	17.0	136.5
2000–2017	May	7.9	21.6	66.2	3.0	72.4	21.1	136.3
	June	13.8	28.0	66.1	2.8	88.0	23.8	170.2
	July	17.2	31.1	66.4	2.7	61.8	23.4	184.5
	August	15.6	29.5	67.7	2.6	56.1	20.5	158.1
	September	9.7	25.5	65.1	2.7	38.8	16.6	122.4

2.2.2. Data Collection

Canopy temperature measurements were recorded at 4 min intervals from full canopy closure until crop senescence for each growing season. Canopy temperature was measured using

CWS220 wireless infrared radiometers (Campbell Scientific, Logan, Utah, USA), which are wireless versions of the SI-111 infrared radiometers (Apogee Instruments, Logan, Utah, USA). The sensors operate over an 8–14 μm spectral range, with a 22° half-angle field of view, and an absolute accuracy of ±0.2 °C over the −10 to 65 °C temperature range. The CWS220 sensors were equipped with a pair of rechargeable batteries and a solar panel for power. The IRTs were mounted on poles and maintained approximately 1 m above the crop canopy, with the sensors oriented toward the canopy at a zenith angle of 45° in the northeast direction. The sensors measured target surface temperature and transmitted the data as radio frequency signals to a 900 MHz 3 dBd omnidirectional antenna (Campbell Scientific), which was installed outside the field on a tall post to ensure that it remained above the plant canopy and could reliably receive signals from all sensors. The antenna was connected to a wireless sensor base station (CWB100, 900 MHz, Campbell Scientific, Logan, Utah, USA), which received and decoded the transmitted radio signals before transferring the data to a CR800 datalogger (Campbell Scientific, Logan, Utah, USA). All IRT sensors were factory-calibrated by the manufacturer before field installation. Each replicate of every treatment (FIT, 60% FIT, and rainfed) had a sensor installed in the middle of the experimental plot.

2.2.3. Data Analysis

Weather and T_c data from 2018, 2019, and 2020 growing seasons were quality-checked before merging into unified analytical datasets. Dates containing negative T_a readings during the 11:30–17:30 h analysis period were excluded. The 1-min weather observations were averaged to 4-min intervals to match the temporal resolution of the dataset. The resulting 4-min weather data were then merged with the corresponding observations based on timestamp. VPD was computed as the difference between saturated vapor pressure and actual vapor pressure (Allen et al., 1998),

$$VPD = e_s - e_a \quad (2.2)$$

where VPD is the vapor pressure deficit (kPa), e_s is the mean saturated vapor pressure (kPa), and e_a is the actual vapor pressure (kPa).

2.2.3.1. Non-Water-Stressed Canopy Temperature and Dynamic Baseline Development

Non-water-stressed canopy temperature ($T_{c,ns}$) was calculated at each 4-min timestamp as the mean of the IRT measurements from the three FIT replicate blocks within each year. This averaging produced one representative non-water-stressed canopy temperature for NWSB development at each timestamp. The corresponding non-water-stressed canopy-to-air temperature difference was calculated as:

$$\Delta T_{ns} = T_{c,ns} - T_a \quad (2.3)$$

where ΔT_{ns} is the non-water-stressed canopy-air temperature difference (°C), $T_{c,ns}$ is the non-water-stressed canopy temperature (°C), and T_a is the air temperature at 3 m height (°C).

After the $T_{c,ns}$ and weather datasets were merged using corresponding 4-min timestamps, each merged observation was assigned to soybean growth stages using year-specific calendar-date ranges derived from field-recorded phenological observations. For each growing season, the date on which a growth stage was first recorded marked the beginning of that stage, and observations from the date through the day preceding the next recorded growth stage were assigned to that stage. Growth-stage assignments were performed separately each year to account for differences in planting dates and crop development among seasons. Within each growth stage, observations collected following canopy closure were then organized into 20 sequential candidate TOD measurement periods labeled at 15-min intervals between 12:00 and 17:00 h, beginning with 12:00–12:15 h and ending with 16:45–17:00 h. To account for gradual diurnal variation in the $(T_c - T_a)$ – VPD relationship, each labeled candidate TOD period was evaluated using a 30-min centered moving window rather than as an isolated 15-min interval. Specifically, each candidate

TOD period was extended by 7.5 min on either side, so that adjacent periods overlap and share observations. This centered moving-period procedure preserved temporal continuity while allowing a locally defined NWSB to be estimated for each candidate TOD period. The same set of candidate TOD periods was subsequently applied separately within each soybean growth stage.

The NWSB was estimated as an empirical relationship between ($T_{c,ns} - T_a$) and VPD, following the approach described by Idso et al. (1981). For each growth stage and candidate TOD period, the NWSB was computed as:

$$\Delta T_{ns,ijsw} = \beta_{0,sw} + \varphi_{0j} + \beta_{1,sw} \cdot VPD_{ijsw} + \varepsilon_{ijsw} \quad (2.4)$$

$$\varphi_{0j} \sim N\left(0, {\delta_{year}}^2\right) \quad (2.5)$$

$$\varepsilon_{ijsw} \sim N\left(0, {\delta_{\varepsilon}}^2\right) \quad (2.6)$$

where $\Delta T_{ns,ijsw}$ is the non-water-stressed canopy-to-air temperature difference (°C) for observation i, year j, growth stage s, and candidate TOD period w; β_0 is the fixed intercept for growth stage s and TOD period w; $\beta_{1,sw}$ is the fixed slope relating VPD to ($T_c - T_a$); φ_{0j} is the random intercept associated with year j; and ε_{ijsw} is the residual error term. The year random effect and residual error were assumed to follow normal distributions specified in Equations 2.5 and 2.6, respectively. Thus, for each target year, NWSB coefficients were estimated using data from the remaining years within the same growth stage and TOD period. After obtaining the intercept and slope relating ($T_c - T_a$) and VPD for each growth stage and TOD measurement period, the NWSB for each observation was predicted using Equation 2.7:

$$NWSB_{ijsw} = \hat{\beta}_{0,sw} + \hat{\beta}_{1,sw} \cdot VPD_{ijsw} \quad (2.7)$$

where $NWSB_{ijsw}$ is the predicted lower baseline temperature difference for observation i in year j, growth stage s, and TOD w.

A leave-one-year-out strategy was used to prevent the baseline for a given year from being evaluated using observations from that same year. The availability of observations differed across growth stages after data filtering, which influenced the model structure used for the NWSB estimation. Because canopy-temperature measurement did not begin at the same growth stage in all years, observation availability for the NWSB estimation varied among growth stages. T_c measurements in 2018 began later in the season than those in 2019 and 2020, which limited the availability of the early-stage data across years. For all three growing seasons, the reproductive stages (R1–R6) were retained in the multi-year analysis. The NWSB for each TOD period was modeled using a linear mixed-effect model described in Equation 2.4 with year treated as a random effect to account for interannual variability within the leave-one-out framework. In contrast, vegetative stages V5 through V7 did not have sufficient cross-year support observations to justify mixed-effect modeling, primarily because 2018 observations were not available at those stages since data collection using IRTs began at later growth stages. Therefore, the lower baselines for V5–V7 were estimated using a linear regression model between $(T_c - T_a)$ and VPD since no data were available at these stages during the 2018 growing season. This strategy ensured that the model complexity remained aligned with the amount and structure of the available data.

2.2.3.2. Best TOD Measurement Period Identification Using Bayesian Modeling

For each observation recorded by the IRT sensor, the observed canopy-air temperature difference was computed as:

$$\Delta T_{ijsw} = T_{c,ijsw} - T_{a,ijsw} \tag{2.8}$$

where ΔT_{ijsw} is the observed $(T_c - T_a)$ (°C) for observation i, year j, growth stage s, and time-of-day measurement period w, $T_{c,ijsw}$ is the canopy temperature (°C) and $T_{a,ijsw}$ is the air temperature (°C). The CWSI was computed as:

$$CWSI_{ijsw} = \frac{\Delta T_{ijsw} - NWSB_{ijsw}}{UB_{sw} - NWSB_{ijsw}} \quad (2.9)$$

where $CWSI_{ijsw}$ is the crop water stress index for observation i, $NWSB_{ijsw}$ is the estimated lower baseline, and UB_{sw} the upper baseline corresponding to the growth stage s and TOD measurement period w, representing fully stressed conditions.

A constant upper baseline of 4 °C was adopted for CWSI computation across all years, growth stages, and candidate TOD periods. This value is consistent with the upper baseline used in a previous study under similar field conditions by Nakabuye et al. (2022). Importantly, fixing the upper baseline as a constant was a deliberate study design decision, because the objective of this study was to identify the best time-of-day measurement period for the lower baseline estimation. Allowing both baselines to vary would have made it difficult to attribute the differences in CWSI predictive performance to the lower baseline specifically. By holding the upper baseline constant, any variation in CWSI and its relationship with yield can be unambiguously attributed to differences in the estimated lower baseline, thereby enabling a clean comparison across candidate TOD periods. Computed CWSI values were constrained to the interval [0, 1], where 0 indicated a non-water-stressed condition and 1 indicated a fully stressed condition. Mean CWSI values were then summarized by year, growth stage, and candidate TOD period and joined with corresponding yield data.

Candidate TOD periods were evaluated separately for each soybean growth stage using Bayesian hierarchical regression models relating mean CWSI to yield across 2018, 2019, and 2020 growing seasons as specified in Equations 2.10 and 2.11. Candidate TOD period performance was assessed using root mean square error (RMSE) of the CWSI-yield relationship, with lower RMSE indicating better predictive performance. The hierarchical modeling framework adopted allowed partial pooling across years while retaining interannual variability in the CWSI-yield relationship

and candidate TOD measurement-period-specific performance (Cressie & Wikle, 2011; Gelman et al., 2013). For each growth stage, the model was specified as

$$Y_i \sim N(\mu_i, \delta^2) \tag{2.10}$$

$$\mu_i = \gamma_0 + \gamma_1 \cdot CWSI + b_{0,year(i)} + b_{1,period(i)} \cdot CWSI \tag{2.11}$$

where Y_i is the observed yield for observation i, μ_i is the expected yield, γ_0 is the population-level intercept, γ_1 is the population-level effect of CWSI, $b_{0,year(i)}$ is the random intercept for year, $b_{1,period(i)}$ is the time-period-specific random slope on CWSI, and δ^2 is the residual variance. The random effects were assumed to follow:

$$b_{0,year(i)} \sim N\left(0, {\tau_{year}}^2\right) \tag{2.12}$$

$$b_{1,period(i)} \sim N\left(0, {\tau_{period}}^2\right) \tag{2.13}$$

Weakly informative prior distributions were specified as $\gamma_0 \sim \text{Normal}(0,50)$, $\gamma_1 \sim \text{Normal}(0,20)$, $\delta \sim \text{Exponential}(1)$, $\tau_{year} \sim \text{Exponential}(1)$, and $\tau_{period} \sim \text{Exponential}(1)$. These priors were considered weakly informative relative to the scale of the observed yield values (Mg ha^{-1}) and CWSI, placing minimal constraints on the posterior while regularizing against implausibly large parameter values. Posterior distributions of RMSE were generated for each candidate TOD period using Markov chain Monte Carlo sampling (van Ravenzwaaij et al., 2018). For each posterior draw, predicted yield values were generated for each candidate TOD measurement period, and RMSE was calculated as

$${RMSE^{(m)}}_w = \sqrt{\frac{1}{n_w} \cdot \sum_{i=1}^{n_w} (Y_i - {\hat{Y}^{(m)}}_{iw})^2} \tag{2.14}$$

where ${RMSE^{(m)}}_w$ is the RMSE for candidate TOD measurement period w at posterior draw m, Y_i is the observed yield, ${\hat{Y}^{(m)}}_{iw}$ is the corresponding posterior-predicted yield, and n_w is the number of observations associated with candidate TOD period w.

RMSE was selected as the evaluation metric because it provides a direct measure of prediction error in the same units as yield, and as a squared-error-based statistic, penalizes larger residuals more strongly. This makes it particularly suitable for identifying the TOD measurement period that yields the most accurate and stable CWSI–yield relationship. A conceptually similar approach has been used by Hernandez et al. (2023) in identifying optimal time frames for soybean yield prediction. For each candidate period, the posterior mean RMSE and its 90% credible interval were calculated to characterize expected predictive performance and associated uncertainty (Kruschke, 2014). The posterior distributions allowed candidate TOD periods to be compared probabilistically while accounting for uncertainty rather than solely based on point estimates. Because a constant upper baseline was used across all years, growth stages, and candidate TOD measurement periods, differences in predictive performance among candidate periods were attributed primarily to variation in the estimated NWSB. For each growth stage, the candidate TOD period with the lowest posterior mean RMSE was identified as the best TOD period for NWSB development. The 90% credible interval and posterior probability of producing the lowest RMSE were used to quantify the uncertainty and strength of support for the selected period.

To provide a fixed benchmark across all growth stages for comparing the identified TOD periods, the 14:00–15:00 h candidate period was designated as the conventional TOD period. This period was adopted from Nielsen (1990), who selected this early-afternoon period because infrared canopy-temperature measurements required unobscured solar conditions and this period generally preceded the rapid development of convective cumulus clouds in the central Great Plains. The comparison was conducted to quantify whether use of a single fixed early-afternoon period produced CWSI–yield model performance comparable to that obtained using the selected growth-stage-specific TOD periods. For each growth stage, the RMSE for the conventional TOD period

at posterior draw m was obtained and the mean RMSE was computed. The percentage increase in posterior mean RMSE associated with the conventional period relative to the selected best TOD period was calculated as:

$$RMSE_{increase,s}(\%) = \frac{RMSE_{conv,s} - RMSE_{best,s}}{RMSE_{best,s}} \cdot 100 \quad (2.15)$$

All data processing and statistical analyses were conducted in RStudio using R version 4.5.2 (R Core Team, 2025). Data import and preparation were performed using the readxl, dplyr, tidyr, purrr, tibble, janitor, stringr, and lubridate packages. Data visualization was conducted using the ggplot2 package. Bayesian hierarchical models were fitted using the brms package with rstan as the computational backend, and posterior summaries were obtained using the posterior package. The lme4 and performance packages were used for mixed-model fitting, evaluation, and diagnostics.

2.3. Results

2.3.1. Irrigation Effects on Soybean Yield

Soybean yield response to irrigation varied among years (Tables 2.2 and 2.3). In 2018, FIT and 60% FIT produced 5.61 and 5.28 Mg ha^{-1}, respectively, and differed significantly ($P < 0.05$) from the rainfed yield of 4.12 Mg ha^{-1}, although FIT and 60% FIT yields did not differ significantly ($P > 0.05$) (Table 2.3). Similar observations were reported by Ashley and Ethridge (1978), Heatherly (1983), and Eck et al. (1987), who showed that soybean can tolerate moderate or temporary water limitation when stress does not coincide strongly with the most sensitive reproductive stages. In 2019, no statistically significant differences ($P > 0.05$) in yield were observed among irrigation treatments, with yields of 4.60, 4.56, and 4.46 Mg ha^{-1} under rainfed, 60% FIT, and FIT, respectively. Irrigation effects were most pronounced in 2020, when yields declined from 5.18 Mg ha^{-1} under FIT to 4.03 Mg ha^{-1} under 60% FIT and 2.97 Mg ha^{-1} under

rainfed conditions, with all treatment means showing statistically significant differences ($P < 0.05$). Thus, irrigation increased yield in 2018 and 2020, but the magnitude of the response was substantially greater in 2020, whereas no measurable irrigation response occurred in 2019.

Table 2.3. Seasonal total irrigation amount (I, mm) and soybean yield (Mg ha^{-1}) for FIT, 60% FIT, and rainfed treatments in 2018, 2019, and 2020. Yield values are mean ± standard error. Different letters within a year indicate significant differences among treatments at $P < 0.05$.

Year	Treatment	Irrigation (mm)	Yield (Mg ha^{-1})
2018	FIT	173	5.61 ± 0.12a
	60% FIT	104	5.28 ± 0.47a
	Rainfed	0	4.12 ± 0.23b
2019	FIT	61	4.46 ± 0.21a
	60% FIT	37	4.56 ± 0.08a
	Rainfed	0	4.60 ± 0.17a
2020	FIT	241	5.18 ± 0.11a
	60% FIT	145	4.03 ± 0.44b
	Rainfed	0	2.97 ± 0.08c

2.3.2. Best Time-of-Day Measurement Period for NWSB Development

The TOD measurement period associated with the lowest posterior mean RMSE differed among soybean growth stages (Figures 2.1 and 2.2). During vegetative development, the best TOD measurement period shifted progressively earlier, from 15:15–15:30 at V5 to 14:45–15:00 at V6 and 14:00–14:15 at V7 (Figure 2.1). The corresponding posterior mean RMSE values were 0.616, 0.605, and 0.368 Mg ha^{-1}, while the posterior probabilities that the best TOD measurement period produced the lowest RMSE among the evaluated candidates were 0.39, 0.718, and 0.84, respectively. Thus, posterior probability increased from V5 to V7 as the best TOD measurement period moved from the late afternoon to the early afternoon. The shapes of the vegetative-stage RMSE profiles also differed (Figure 2.1). At V5, several afternoon periods produced similarly low RMSE values, and their 90% credible intervals overlapped substantially, indicating limited

evidence that any one period performed clearly better than the neighboring periods. The minimum became more clearly defined at V6, although nearby periods remained competitive. At V7, RMSE increased more sharply on either side of 14:00–14:15, providing stronger differentiation between the selected period and the surrounding candidates. At R1, the selected period shifted to 12:30–12:45, with a posterior mean RMSE of 0.456 Mg ha^{-1}; however, its posterior probability of 0.23 was the lowest among the evaluated stages, reflecting a broad region of comparable performance around midday and early afternoon.

For the remaining reproductive stages, the selected periods were confined to a relatively narrow interval between 12:00 and 13:15 (Figure 2.2). The best-performing periods were 12:00–12:15 at R2, 12:15–12:30 at R3, 13:00–13:15 at R4, 12:00–12:15 at R5, and 13:00–13:15 at R6. Posterior mean RMSE values for these stages were 0.507, 0.464, 0.579, 0.340, and 0.302 Mg ha^{-1}, respectively, with corresponding posterior probabilities of 0.89, 0.57, 0.93, 0.50, and 0.404. The most clearly defined reproductive-stage minimum occurred at R4, followed by R2, whereas the profiles at R3, R5, and R6 contained several nearby periods with similar RMSE values. Across all growth stages, the selected TOD periods ranged from 12:00–12:15 at R2 and R5 to 15:15–15:30 at V5, while posterior mean RMSE ranged from 0.302 Mg ha^{-1} at R6 to 0.616 Mg ha^{-1} at V5 (Figures 2.1 and 2.2). Posterior support was strongest at R4, R2, and V7, with probabilities of 0.93, 0.89, and 0.84, respectively, and weakest at R1, V5, and R6, with probabilities of 0.23, 0.39, and 0.404. These results showed that the degree of separation among candidate periods varied by growth stage: some stages had a distinct RMSE minimum, whereas others had several adjacent periods with comparable predictive performance. Overall, vegetative stages favored mid- to late-afternoon measurements, while reproductive stages were concentrated closer to midday and early afternoon.

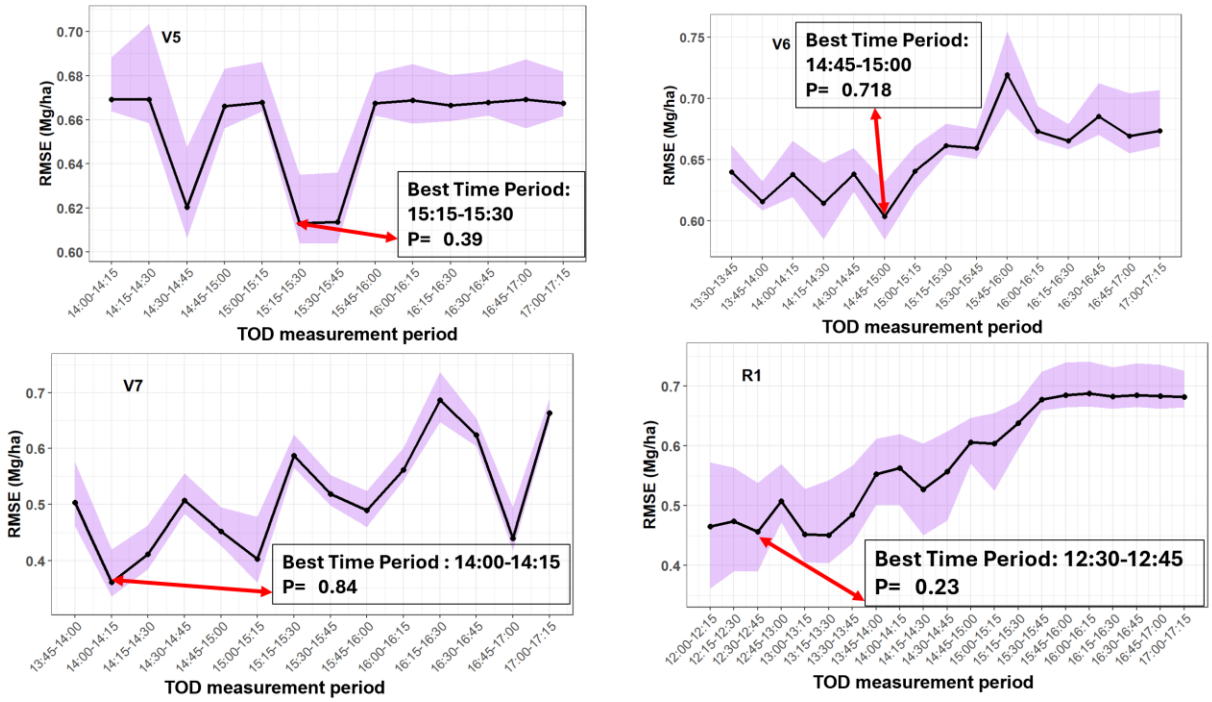


Figure 2.1. Measurement-period-specific RMSE posterior distribution profiles used to identify the best time-of-day (TOD) measurement period for NWSB performance during the late vegetative stages (V5, V6, and V7) and the early reproductive stage (R1). The black line shows the estimated RMSE for each 15-min time-of-day period, and the shaded purple band represents the 90% credible interval from the Bayesian analysis. The red arrow indicates the selected best measurement period, and the inset box reports the posterior probability.

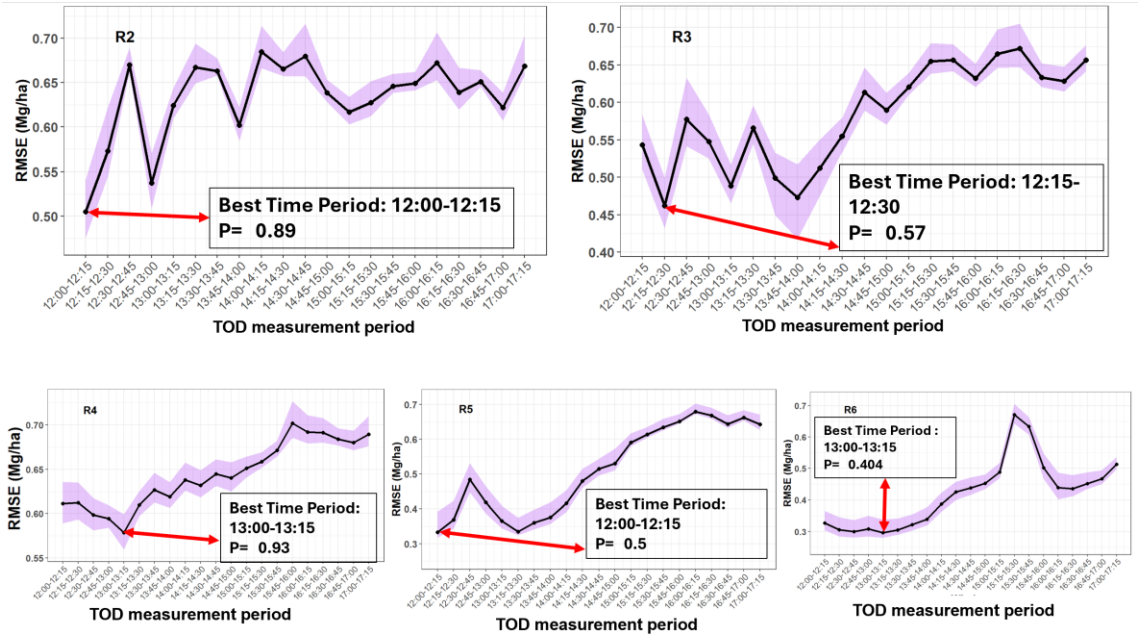


Figure 2.2. Time-period-specific posterior RMSE profiles for identifying the best TOD measurement period for NWSB development during reproductive stages R2–R6. The black line represents posterior mean RMSE, the shaded band indicates the 90% credible interval, and the red arrow marks the selected best TOD measurement period with its posterior probability shown in the inset.

The selected growth-stage-specific periods were subsequently compared with the conventional fixed period of 14:00–15:00 h, corresponding to 13:00–14:00 MDT (Table 2.4) as adopted from Nielsen (1990). During vegetative development, use of the conventional period increased posterior mean RMSE from 0.616 to 0.659 Mg ha^{-1} at V5, from 0.605 to 0.625 Mg ha^{-1} at V6, and from 0.368 to 0.437 Mg ha^{-1} at V7. These differences represented relative increases in RMSE values of 7.0, 3.3, and 18.7%, respectively. The smallest difference among all evaluated stages occurred at V6, whereas the largest vegetative-stage difference occurred at V7. The performance difference was generally greater during reproductive development (Table 2.4). Relative increases in RMSE associated with the conventional period were 23.9% at R1, 32.1% at R2, 22.6% at R3, 10.4% at R4, 43.0% at R5, and 41.8% at R6. The largest increases occurred at R5 and R6, where posterior mean RMSE rose from 0.340 to 0.487 Mg ha^{-1} and from 0.302 to

0.428 Mg ha^{-1}, respectively, whereas R4 had the smallest reproductive-stage increase. Across all stages, the conventional fixed period produced posterior mean RMSE values that were 3.3–43.0% higher than those obtained using the selected best TOD measurement periods across growth stages.

The relationship between the selected and conventional periods also varied by growth stage. At V5, the selected period occurred later than the conventional interval, while the V6 and V7 best TOD measurement periods were within the conventional period. In contrast, all reproductive-stage selections occurred before the conventional 14:00–15:00 h interval, with most concentrated between 12:00 and 13:15. The greatest RMSE increases were generally observed at stages for which the selected period was separated most clearly from the conventional interval, particularly R2, R5, and R6. Conversely, smaller differences occurred at V6 and R4, where the selected periods were either within or closer to the conventional measurement period. Overall, the comparison showed that the magnitude of the RMSE increase associated with the conventional period depended on both growth stage and the temporal distance between the conventional and selected measurement periods.

Table 2.4. Posterior mean RMSE of the CWSI–yield relationship for the selected growth-stage-specific best TOD periods and the conventional fixed 14:00–15:00 h period in soybean. Conventional penalty represents the percentage increase in RMSE relative to the selected best TOD period.

Growth stage	Selected TOD period	Selected RMSE (Mg ha^{-1})	Conventional period	Conventional RMSE (Mg ha^{-1})	Conventional penalty (%)
V5	15:15–15:30	0.616	14:00–15:00	0.659	7.0
V6	14:45–15:00	0.605	14:00–15:00	0.625	3.3
V7	14:00–14:15	0.368	14:00–15:00	0.437	18.7
R1	12:30–12:45	0.456	14:00–15:00	0.565	23.9
R2	12:00–12:15	0.507	14:00–15:00	0.670	32.1
R3	12:15–12:30	0.464	14:00–15:00	0.568	22.6
R4	13:00–13:15	0.579	14:00–15:00	0.639	10.4
R5	12:00–12:15	0.340	14:00–15:00	0.487	43.0
R6	13:00–13:15	0.302	14:00–15:00	0.428	41.8

2.3.3. Growth-Stage-Specific NWSBs at the Best Time-of-Day Measurement Periods

The growth-stage-specific NWSBs developed using observations collected during the selected TOD measurement periods showed negative linear relationships between $(T_c - T_a)$ and VPD at all soybean growth stages (Figure 2.3). These negative linear relationships were consistent with previously reported soybean NWSBs (Candogan et al., 2013; Jackson et al., 1981; Morales-Santos & Nolz, 2023; Nielsen, 1990). Inverse $(T_c - T_a)$–VPD relationships have also been reported for other crops, including squash and alfalfa (Idso et al., 1981), bell pepper (Idso et al., 1990), sunflower (Nielsen, 1994), wheat (Alderfasi & Nielsen, 2001), watermelon (Orta et al., 2003), tall fescue (Al-Faraj et al., 2000), and potato (Ekinzog et al., 2022). More broadly, Idso (1982) compiled negative-slope NWSBs for numerous well-watered plant species. Thus, the direction of the relationships obtained in this study agreed with the established empirical pattern, whereas the stage-specific variation in their fitted coefficients distinguished the present results from season-wide baselines reported previously.

The estimated NWSB slopes ranged from -0.62 to $-1.97\ ^\circ\mathrm{C\ kPa^{-1}}$, while intercepts ranged from -0.75 to $4.40\ ^\circ\mathrm{C}$. The fitted slopes were -1.40, -1.54, and $-0.62\ ^\circ\mathrm{C\ kPa^{-1}}$ at V5, V6, and V7, respectively. During reproductive growth stages, slopes were -1.62, -1.31, -1.52, -1.84, -1.97, and $-1.42\ ^\circ\mathrm{C\ kPa^{-1}}$ at R1, R2, R3, R4, R5, and R6, respectively. The steepest negative relationship occurred at R5, followed by R4, whereas the least negative relationship occurred at V7. Intercepts were -0.21, -0.35, and $-0.75\ ^\circ\mathrm{C}$ at V5, V6, and V7, respectively, and 4.40, 1.14, 0.37, -0.08, 0.65, and $-0.47\ ^\circ\mathrm{C}$ at R1 through R6, respectively. These results showed that both the slope and intercept of the $T_c - T_a$–VPD relationship varied across soybean growth stages.

Growth-stage-specific NWSBs were also compared with previously published soybean baselines. Idso et al. (1981) reported $T_c - T_a = 1.44 - 1.34\,\mathrm{VPD}$, whereas Nielsen (1990), Candogan et al. (2013), Tekelioğlu et al. (2017), and Morales-Santos and Nolz (2023) reported $T_c - T_a = 2.51 - 2.02\,\mathrm{VPD}$, $T_c - T_a = 0.65 - 1.85\,\mathrm{VPD}$, $T_c - T_a = -2.051 - 2.162\,\mathrm{VPD}$, and $T_c - T_a = 3.64 - 2.17\,\mathrm{VPD}$, respectively. It should be noted, however, that these reported soybean NWSBs were seasonal rather than growth-stage-specific baselines. Most slopes obtained in the present study were within or close to the range reported in these earlier studies. In particular, the slopes at R2, V5, and R6; -1.31, -1.40, and $-1.42\ ^{\circ}\mathrm{C\ kPa^{-1}}$, respectively were comparable to the soybean NWSB slope of $-1.34\ ^{\circ}\mathrm{C\ kPa^{-1}}$ reported by Idso et al. (1981). The R4 slope, $-1.84\ ^{\circ}\mathrm{C\ kPa^{-1}}$, closely matched the value of $-1.85\ ^{\circ}\mathrm{C\ kPa^{-1}}$ reported by Candogan et al. (2013), and the R5 slope, $-1.97\ ^{\circ}\mathrm{C\ kPa^{-1}}$, was close to the slope of $-2.02\ ^{\circ}\mathrm{C\ kPa^{-1}}$ reported by Nielsen (1990). In contrast, the V7 slope, $-0.62\ ^{\circ}\mathrm{C\ kPa^{-1}}$, was substantially less negative than most of the published soybean slopes reviewed in this study.

The stage-specific intercepts obtained in this study varied in their agreement with reported soybean baselines in literature. The R5 intercept of $0.65\ ^{\circ}\mathrm{C}$ was identical to that reported by Candogan et al. (2013), while the R2 intercept of $1.14\ ^{\circ}\mathrm{C}$ was relatively close to the $1.44\ ^{\circ}\mathrm{C}$ intercept reported by Idso et al. (1981). The R1 intercept of $4.40\ ^{\circ}\mathrm{C}$ exceeded the values of $3.64\ ^{\circ}\mathrm{C}$ reported by Morales-Santos and Nolz (2023) and $2.51\ ^{\circ}\mathrm{C}$ reported by Nielsen (1990). Conversely, the negative intercepts obtained at V5, V6, V7, R4, and R6 differed from the predominantly positive intercepts reported in most previous soybean studies, although Tekelioğlu et al. (2017) also reported a negative intercept.

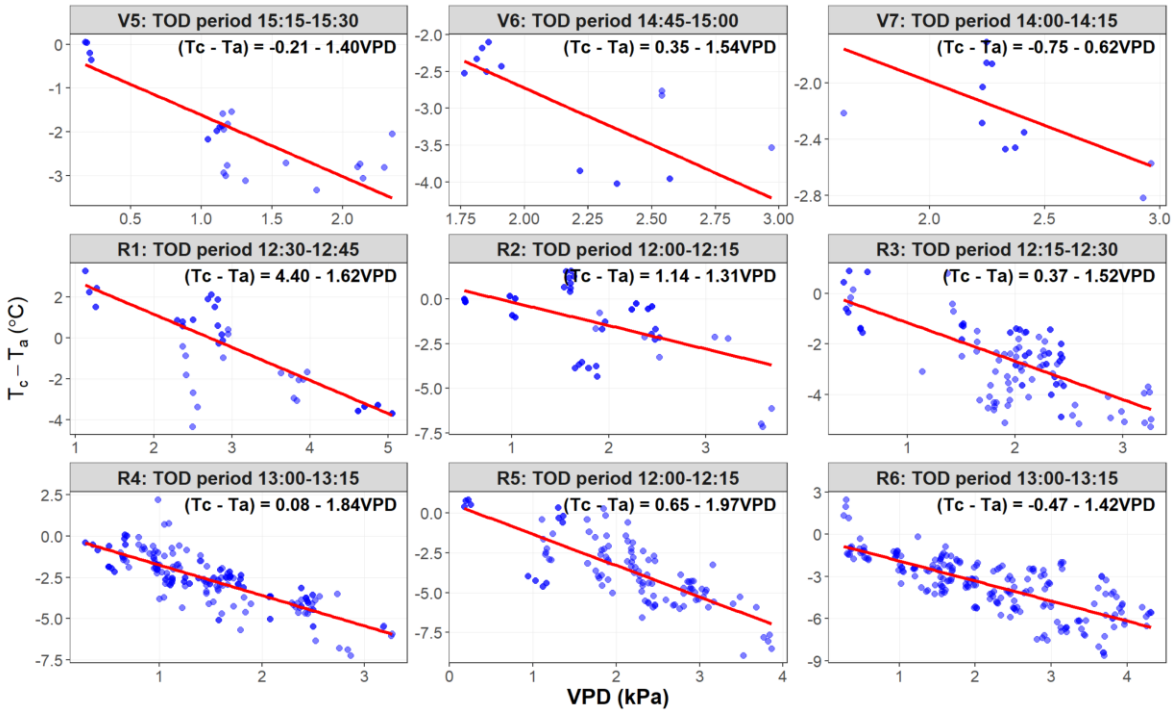


Figure 2.3. Growth-stage-specific NWSBs relating soybean ($\mathbf{T_c - T_a}$) to VPD, developed after identifying the best time-of-day (TOD) measurement period for each growth stage. Vegetative-stage baselines (V5–V7) used the available observations from 2019 and 2020, whereas reproductive-stage baselines (R1–R6) used observations from 2018–2020. Each panel corresponds to one soybean growth stage (V5 to R6) and its selected best TOD period. Blue points represent the available pooled ($\mathbf{T_c - T_a}$) and VPD observations from the three years, red lines show the fitted stage-specific linear NWSBs, and the displayed equations are the resulting pooled baseline relationships.

2.4. Discussion

The variation in irrigation response to yield among years indicated that yield was strongly influenced by seasonal water availability and evaporative demand (Table 2.3). The similarity in yield between FIT and 60% FIT treatments in 2018 suggests that the crop water requirement under deficit irrigation (60% FIT) was sufficient to avoid yield-limiting stress during sensitive reproductive periods. The findings of Eck et al. (1987) and Heatherly (1983), which showed that soybean can tolerate moderate or temporary water deficit when stress does not coincide with critical yield-forming growth stages, further help explain the similar yields observed between the

two treatments in 2018. It should be noted, however, that similar yields do not necessarily indicate that both treatments experienced similar consumptive water use, but rather the differences in irrigation level did not result in a statistically detectable yield response under the conditions of that growing season.

The absence of an irrigation effect on yield in 2019 can be attributed to seasonal weather conditions. This year had above normal precipitation and below normal ET_o relative to the long-term average (Table 2.2). Relatively high precipitation during July and August likely maintained adequate soil water availability during the reproductive growth stages, including flowering, pod development, and seed filling, thereby reducing crop dependence on irrigation. Under these conditions, additional irrigation would not be expected to increase yield substantially, consistent with the findings of Lee et al. (2025). Candogan et al. (2013), Irmak et al. (2014), and Xie et al. (2024) reported similar year-dependent irrigation effects on yield and attributed them to differences in precipitation amount and distribution, soil water content, crop water use, and timing of water deficits relative to crop development. In contrast, the pronounced irrigation response in 2020 was consistent with substantially drier and more evaporatively demanding conditions. June and August were particularly dry, and both months were characterized by relatively high T_{max}, low RH_{avg}, and high ET_o (Table 2.2). These conditions likely increased crop water demand and caused the crop to strongly depend on irrigation. The progressive reduction in yield from FIT to 60% FIT and from 60% FIT to rainfed conditions suggest that the available water under the latter treatments was insufficient to fully satisfy crop demand. Water deficits during reproductive development can reduce pod retention, seed number, and individual seed weight, resulting in substantial yield losses (Dogan et al., 2007; Doss et al., 1974; Foroud et al., 1993; Karam et al., 2005). Collectively, the contrasting seasons provided a useful range of crop water conditions for evaluating whether CWSI

calculated using different TOD measurement periods retained a meaningful relationship with final yield.

The dependence of the best TOD measurement period on soybean growth stage indicates that the thermal conditions most informative for representing yield-relevant water stress were not constant throughout crop development. However, this pattern should not be interpreted to mean that growth stages influenced the timing of peak solar radiation (Allen et al., 1998). Solar radiation provides energy input, whereas T_c reflects how the crop intercepts and partitions that energy between evapotranspiration and sensible heating as the crop develops (Idso et al., 1981; Sauer et al., 2007). Changes in leaf area, canopy architecture, canopy height, soil exposure, and aerodynamic properties during soybean development may alter the thermal response of the canopy to the same diurnal atmospheric forcing as reported by Blad and Baker (1972). Sauer et al. (2007), for example, showed that a fully developed soybean canopy intercepted nearly 90% of incoming shortwave and net radiation and partitioned more than 80% of the available energy to evapotranspiration. Similarly, the observation by Jeffers and Shibles (1969) that soybean canopy response to radiation depended on leaf area further provides a plausible explanation for growth stage dependence on the best TOD measurement period for NWSB development. Soybean canopies at different developmental stages may experience similar external radiative forcing but differ in the TOD at which T_c most effectively represents crop water status.

The transition from late afternoon TOD measurement periods during vegetative growth stages to periods closer to midday and early afternoon during reproductive development may reflect developmental changes in the TOD at which soybean water relations are most strongly coupled with atmospheric demand. Field-grown soybean exhibits pronounced diurnal variation in plant water relations, with light intensity and VPD influencing photosynthesis and water use and

high midday VPD coinciding with reductions in leaf hydraulic conductance and leaf water potential as discussed by Locke and Ort (2015). More directly, Hou et al. (2019) reported that T_c depression and transpiration measured near noon during reproductive development were more strongly related to soybean yield than measurements collected at other TOD. These observations are consistent with the concentration of the best TOD measurement periods identified for the reproductive-stage periods near midday. The variation in the shapes of the posterior RMSE profiles (Figures 2.1 and 2.2) indicates that the certainty of identifying a single TOD measurement period was not uniform across growth stages. Broad profiles suggest that several adjacent periods produced comparable CWSI–yield performance, possibly because they captured similar canopy–atmosphere conditions. This pattern is plausible because T_c, VPD, R_s, and U_3 change progressively throughout the day rather than abruptly (Payero et al., 2005a; Peters & Evett, 2004). In contrast, sharply defined profiles indicate stronger statistical differentiation among candidate periods, although they should not be interpreted as evidence of a unique physiological optimum. Meteorological variability, including intermittent cloud cover, low VPD, and fluctuations in radiation or wind, also could have influenced the degree of separation among periods by altering T_c independently of soil water status.

The negative slopes obtained from the derived NWSBs across all growth stages aligned with the expected response of a well-watered crop canopy (Idso, 1982; Jackson, 1982; Jackson et al., 1981). However, the most important finding was that the magnitude of this response, represented by the slope and intercept of the NWSBs, differed among growth stages. These differences among baselines will likely result in different CWSI values from the same T_c and VPD observations. The agreement between some stage-specific coefficients and published seasonal NWSBs suggests that these baselines can reasonably represent canopy behavior during certain

growth stages. Differences at other stages likely reflect developmental, environmental, and measurement-timing effects that are masked by being averaged when a single baseline is developed for the entire season.

Overall, the growth stage-dependent selection of TOD measurement periods suggests that a single fixed TOD measurement period may overlook crop developmental changes in the relationships among ($T_c - T_a$), VPD, crop water status, and yield. This approach for assessing and identifying the best TOD measurement period using a Bayesian framework and yield as a response variable presents a way to improve CWSI estimation and irrigation water management. The stage-specific TOD approach has practical relevance for both infrared thermometry and UAV-based thermal imaging because the selected measurement time determines the canopy–atmosphere conditions represented by the thermal observations. For continuous infrared thermometers, the identified periods can guide the selection of observations for NWSB development, whereas for handheld infrared thermometers and UAVs, they can guide the timing of field measurements and image acquisition. However, the periods identified here are conditional on the study conditions and should be validated across environments and relative to local solar time. Future research should extend this approach to other crops and establish standardized protocols for selecting the best TOD measurement period, thermal data acquisition, and NWSB development.

2.5. Conclusions

This study established an approach for identifying TOD measurement periods for soybean non-water-stressed baseline (NWSB) development and demonstrated that both measurement timing and baseline characteristics vary with crop growth stage. Vegetative stages (V5–V7) exhibited weaker relationships and were best represented by mid- to late-afternoon periods, whereas reproductive stages (R1–R6) were generally better represented by periods closer to solar

noon and early afternoon. These stage-specific differences indicate that the conventional 14:00–15:00 h measurement period may not be equally suitable for CWSI estimation throughout soybean development.

The fitted NWSBs also differed among growth stages, as reflected by changes in the slope and intercept of the $(T_c - T_a)$–VPD relationship. Collectively, these findings suggest that the soybean NWSB is not a fixed seasonal relationship but varies with crop development and environmental changes. This study shows that using a fixed TOD measurement period for the entire growing season may not always provide the most representative NWSB for CWSI estimation. Future research should evaluate this framework across additional crops and environments to determine whether stage-specific measurement periods and corresponding baselines can improve the reliability of crop water stress assessment for irrigation management.

Chapter 3 - Dynamic Data-Based Mechanistic Modeling of Non-Water-Stressed Maize Canopy Temperature for Crop Water Stress Index Estimation

Abstract

Reliable estimation of non-water-stressed canopy temperature ($T_{c,ns}$) is central to empirical crop water stress index (CWSI) calculation, yet obtaining this reference under field conditions without a continuously maintained well-watered treatment remains a practical barrier. This study developed and evaluated a data-based mechanistic (DBM) dynamic modeling framework for predicting maize $T_{c,ns}$ under semiarid field conditions and assessed predictive performance across phenological growth stages. The model was formulated as a first-order continuous-time transfer function driven by air temperature, solar radiation, and vapor pressure deficit, with parameters identified using the recursive refined instrumental-variable algorithm. Cross-year transferability was evaluated across three growing seasons at North Platte, Nebraska, USA, by applying parameters identified in one season without modification to independent seasons. Predictive performance varied systematically with growth stage. At the milk (R3) and dough (R4) stages, mean absolute error ranged from 0.093 to 0.342 °C and the coefficient of determination (R^2) ranged from 0.686 to 0.958 across the reported evaluations. Performance was weaker at V8, V9, and the blister stage (R2), where mean absolute error ranged from 0.250 to 0.442 °C and R^2 ranged from 0.391 to 0.503. The results show that a physically interpretable dynamic framework can predict $T_{c,ns}$ from standard weather variables without a dedicated reference treatment, but its cross-year reliability remains growth-stage dependent.

Keywords: continuous-time system identification; refined instrumental variable; cross-year validation; model transferability; vapor pressure deficit; semiarid agriculture.

3.1. Introduction

Canopy temperature (T_c) reflects the thermal state of the crop canopy as determined by exchanges of sensible and latent heat with the surrounding environment. Although it does not measure plant water status directly, it serves as an important proxy because of its inverse relationship with transpiration and stomatal conductance (Jones, 1999; Urban et al., 2017). As water becomes limiting and stomata close, evaporative cooling declines and T_c increases, making continuous thermal monitoring a useful approach for detecting crop water stress (Jackson, 1982; Mahan et al., 2015; Morales-Santos & Nolz, 2023). To improve interpretation of T_c under varying atmospheric conditions, Idso et al. (1981) developed the crop water stress index (CWSI), which expresses crop stress relative to non-water-stressed and non-transpiring baseline conditions. Since then, canopy temperature measured with infrared thermometers, often interpreted through CWSI-based or related thermal stress approaches, has been used for irrigation scheduling in various irrigated crop systems, including maize (Geiser et al., 1982; Nakabuye et al., 2022; Sadler et al., 2002). In semi-arid and water-limited regions where producers must sustain yield while coping with increasing pressure on freshwater resources, this nondestructive method could be valuable in supporting timely irrigation decisions because it provides rapid, plant-centered information on crop response.

The CWSI approach for monitoring crop water status, however, relies on both the non-water-stressed baseline and an upper reference baseline to define the thermal limits of well-watered and fully stressed canopy conditions, respectively. In this framework, CWSI can be computed as shown in Equation 3.1:

$$CWSI = \frac{(T_c - T_a) - (T_c - T_a)_{LL}}{(T_c - T_a)_{UL} - (T_c - T_a)_{LL}} \quad (3.1)$$

where T_c is the observed canopy temperature, T_a is air temperature, $(T_c - T_a)_{LL}$ is the lower limit representing a non-water-stressed canopy, and $(T_c - T_a)_{UL}$ is the upper limit for a non-transpiring or fully stressed canopy. The concept of the non-water-stressed baseline was advanced through the complementary work of Idso et al. (1981) and Jackson et al. (1981), with its empirical basis later established by Idso (1982) and its theoretical basis clarified by Jackson (1982). In the empirical formulation, the lower baseline (Lower Limit) is commonly expressed as a linear relationship between canopy-to-air temperature difference $(T_c - T_a)$ and vapor pressure deficit (VPD) under well-watered conditions, as shown in Equation 3.2:

$$(T_c - T_a)_{LL} = a + b \cdot VPD \quad (3.2)$$

where T_c is equivalent to $T_{c,ns}$, the non-water-stressed canopy temperature, and a and b are empirical coefficients describing the intercept and slope of the baseline. Thus, the lower baseline represents the expected thermal behavior of a well-watered crop under a given atmospheric demand.

Despite its central role in defining the lower baseline, $T_{c,ns}$ is not a quantity that is readily available during routine field monitoring. In practical applications of the empirical CWSI approach, $T_{c,ns}$ can be measured directly under well-watered conditions whereby the crop is kept under non-water-stressed conditions (receives 100% of its water requirement) throughout the season (Emekli et al., 2007; Kumari et al., 2024; Nielsen, 1990; Yazar et al., 1999). This requirement complicates implementation because it may necessitate dedicated non-water-stressed treatments, additional sensors or reference targets, and measurement conditions that are sufficiently stable to characterize the thermal response of a fully transpiring canopy thereby increasing costs and operational burden for a producer. Some studies have also noted that the

empirical method is constrained by the need to collect appropriate reference data close to midday and under clear-sky conditions, which limits operational flexibility and hinders automation in irrigation scheduling (Irmak et al., 2000; Katimbo et al., 2022; Nakabuye et al., 2022; Wanjura et al., 2003).

To reduce this burden, some studies have used natural or artificial reference surfaces to approximate non-water-stressed and non-transpiring crop conditions. For example, wet and dry reference surfaces have been proposed so that observed T_c can be compared with temperatures representing maximum and zero transpiration under the same environment (Jones, 2004; Jones et al., 2002; Katimbo et al., 2022; Maes & Steppe, 2012). It has been noted, however, that one of the pitfalls of this method is that simple artificial materials such as filter paper can differ from real leaves in thermal and radiative properties, which can cause their energy balance to depart from that of the crop itself (Grant et al., 2010; Jones et al., 2002; Vialet-Chabrand & Lawson, 2020). To better support real-time CWSI estimation in maize, Apolo-Apolo et al. (2020) designed and evaluated new hemispherical cellulose-paper artificial reference surfaces. These surfaces showed promise for real-time CWSI estimation, although the study also highlighted continuing uncertainty about what exactly such surfaces measure. These considerations make reference-surface methods useful, but not without practical and physical limitations.

An alternative strategy has been to predict $T_{c,ns}$ from meteorological and crop-response variables, thereby reducing reliance on direct reference measurements. Using multiple linear regression, Payero et al. (2005a) developed daytime and near-noon equations to estimate lower baselines for alfalfa and tall fescue, with reported coefficient-of-determination (R^2) values of 0.89 for full-day models and up to 0.92 and 0.94 for near-noon models. In wine grape, King and Shellie (2016) used neural networks to predict well-watered leaf temperature from weather inputs and

reported mean squared error and mean absolute error values of 1.07 and 0.82 °C for 'Syrah' and 1.30 and 0.98 °C for 'Malbec', respectively. They also reported that neural-network predictions were less variable than those obtained from multiple linear regression using the same predictors. In maize, Nakabuye et al. (2024) estimated $T_{c,ns}$ using a weather-based multilinear regression model and found strong agreement between modeled and observed $T_{c,ns}$ across three growing seasons, with a model R^2 of 0.94.

These studies clearly demonstrate that, within a given cropping system, non-water-stressed canopy temperature ($T_{c,ns}$) can be estimated from meteorological variables without maintaining a dedicated reference plot throughout the season. However, these approaches should not be interpreted as universally transferable across crop species, because canopy thermal behavior depends on crop type, canopy architecture, and phenological development (Gu et al., 2021; Idso, 1982; Jones et al., 2009). Most of the reported approaches also remain empirical and static, in the sense that they relate $T_{c,ns}$ to selected meteorological covariates over specified periods rather than explicitly representing the time-varying dynamics of canopy thermal response. That limitation matters because T_c is not governed only by the instantaneous state of weather variables, but by a dynamic interaction among radiation forcing, T_a, atmospheric demand, and plant response. Dynamic model frameworks have been applied to simplify and model complex environmental and biological processes (Taylor et al., 2007; Young, 2006) to predict time-varying natural biological responses (Kirchsteiger et al., 2011). A key advantage of such frameworks is their ability to represent input-specific time delays and time-varying system behavior, rather than assuming that T_c responds instantaneously to environmental forcing. Solar radiation (R_S), T_a, VPD, and wind may affect $T_{c,ns}$ over different lag periods because canopy thermal dynamics are shaped by thermal inertia, stomatal adjustment, and canopy–atmosphere coupling (Al-Faraj et al., 2000; Schymanski

et al., 2013). Consequently, dynamic modeling offers a more process-relevant framework for representing $T_{c,ns}$ than approaches based only on contemporaneous relationships.

In this direction, Adeyemi et al. (2018) applied a dynamic modeling framework to predict the baseline temperatures required for CWSI computation in greenhouse-cultivated lettuce, showing that dynamic modeling could accommodate time-varying plant response through recursive parameter estimation and input-specific delays. Nevertheless, that study was conducted under greenhouse conditions, where the environment was relatively regulated and aerodynamic disturbances were limited. By contrast, recent efforts to predict $T_{c,ns}$ in maize under semiarid conditions have largely relied on regression- and machine-learning-based approaches rather than dynamic modeling. Whether a dynamic framework can reliably predict $T_{c,ns}$ under field conditions remains unclear, particularly for maize grown in semi-arid regions where radiation load, VPD, and canopy-atmosphere interactions vary throughout the day. Moreover, because maize canopy architecture, aerodynamic behavior, and crop-atmosphere coupling change substantially with development, the dynamics governing $T_{c,ns}$ may also vary across growth stages. Therefore, the objective of this study was to develop and evaluate a dynamic data-based mechanistic modeling framework for predicting $T_{c,ns}$ in field-grown maize under semiarid conditions, and to assess how its predictive performance varied across growth stages.

3.2. Materials and Methods

3.2.1. Site Description and Experimental Design

The field study was conducted during the 2018, 2019, and 2020 growing seasons at the University of Nebraska–Lincoln West Central Research, Extension and Education Center (WCREEC) in North Platte, Nebraska, USA (41.1°N, 100.8°W; elevation 861 m above sea level). This region is characterized by a semi-arid climate with 80% of annual precipitation occurring

between late April and mid-October according to Payero et al. (2009). The predominant soil type of this site is Cozad silt loam (Fluventic Haplustoll) with a field capacity of 0.29 $m^3\ m^{-3}$ and permanent wilting point of 0.11 $m^3\ m^{-3}$ (Klocke et al., 1999). The experiment was arranged in a randomized complete block design (RCBD) format with four blocks. Individual plot dimensions were 9.1 m × 72.2 m. This study, however, used only three blocks due to the limited availability of infrared radiometer sensors for data collection. Each experimental block consisted of three treatments: rainfed treatment (hereafter RF), deficit irrigated treatment which received 60% of the full irrigation treatment (hereafter 60% FIT) to induce stress, and the fully irrigated treatment which received 100% of the total crop water requirement (hereafter FIT). The experimental site was irrigated using a subsurface drip irrigation system with drip lines spaced 1.52 m apart and installed at a depth of 0.40 m. Soil water content was monitored using a neutron moisture meter (NMM). The obtained measurements were used to compute maximum allowable depletion (MAD), and FIT irrigation was triggered when soil water depletion reached 50% of MAD.

In each of the 2018, 2019, and 2020 growing seasons, Pioneer 1197 AMT (Corteva Agriscience, Wilmington, Delaware, USA) maize (*Zea mays L.*) was planted at an approximate depth of 5 cm in 0.76 m rows at a seeding rate of 84,000 seeds ha^{-1} under a no-till system after soybean in rotation. Nitrogen (N) fertilizer, which was prescribed based on soil residual N following Shapiro et al. (2019), was applied to the entire field in the form of urea-ammonium nitrate (UAN 32%). A preplant N application of 67.2 kg ha^{-1} was made on 19 April 2018, 17 April 2019, and 21 April 2020 using a double-coulter applicator, with fertilizer placed approximately 19 cm from the planted row on both sides, although spacing and equipment setup varied slightly among years to match field conditions and dripline alignment. At planting, starter fertilizer (10-34-0) was applied at 65 kg ha^{-1} in all years, with the 2020 application placed in-furrow. In addition,

a phosphorus blend was broadcast on 28 April 2020 at 133.0 L ha^{-1} as a blanket application. In-season sidedress N was applied at 179, 157, and 126 kg ha^{-1} in 2018, 2019, and 2020, respectively. Pesticides were applied uniformly, as needed, to the entire field. The crop was harvested on 29 October 2018, 7 November 2019, and 30 October 2020 using a John Deere Model 9500 combine with a calibrated yield monitor.

3.2.2. Instrumentation and Data Collection

Throughout each season, T_c was measured continuously using SI-1H1 and SI-4H1 infrared radiometers (IRT sensors) (Apogee Instruments, Logan, Utah, USA). The IRT sensors were mounted approximately 1 m above the crop canopy at a 45° view angle toward the crop canopy in the plots of FIT, 60% FIT, and RF for each growing season. The IRTs were oriented in the northeast direction to view sunlit canopy during the midafternoon measurement period under unobstructed solar conditions because these periods have been reported to be the best for collecting T_c (DeJonge et al., 2015). The IRTs scanned the temperatures every 6 s, averaged the measurements to 1 min, and logged the data onto CR1000X dataloggers (Campbell Scientific, Logan, Utah, USA). All IRTs were calibrated by the manufacturer prior to field installation. Payero et al. (2005b) described the study area as being located within a semi-arid climatic zone, where evaporative demand during the growing season strongly affects crop irrigation requirements. Consistent with this setting, and because the present study focused on predicting $T_{c,ns}$ from meteorological variables, microclimatic data were obtained from an automatic weather station located approximately 100 m from the experimental site.

The station, North Platte 3SW Beta, is part of the Nebraska Mesonet network and provided measurements of minimum air temperature ($T_{\min}$), maximum air temperature ($T_{\max}$), incoming R_s, and relative humidity (RH); these variables were used in the analysis. Mean meteorological

conditions during the daytime measurement periods for each growth stage are summarized in Table 3.1. Neutron moisture meters (NMM) CPN 503 Elite Hydroprobe and CPN 503DR (InstroTek, CA, USA) were used to measure volumetric soil water content (θ_v) weekly to biweekly from a depth of 0.15–1.80 m in 2018 and to a depth range of 0.15–2.59 m in 2019 and 2020, at increments of 0.30 m. While the CPN 503 Elite Hydroprobe was cross-calibrated to the CPN 503DR with R^2 of 0.994 and RMSE of 0.004 $m^3\ m^{-3}$, the CPN 503DR was gravimetrically calibrated for the site with R^2 of 0.997 and RMSE of 0.010 $m^3\ m^{-3}$ (Lo et al., 2020). One neutron access tube was inserted into a crop row within each of the three treatment plots during the 2018 season. In 2019 and 2020 seasons, two access tubes were installed within each plot per treatment. The paired tubes were spaced 0.38 m perpendicular to the row direction and positioned to evenly straddle a crop row.

Table 3.1. Mean (± standard error) minimum air temperature (T_{min}), maximum air temperature (T_{max}), and incoming solar radiation (R_s) during daytime measurement periods across maize phenological growth stages for the 2018, 2019, and 2020 growing seasons.

Year	Growth stage	T_{min} (°C)	T_{max} (°C)	R_s (W m^{-2})
2018	VT–R1	23.9 ± 0.1	24.1 ± 0.1	477.3 ± 4.7
	R2	23.3 ± 0.1	23.6 ± 0.1	455.2 ± 5.7
	R3	17.9 ± 0.4	18.3 ± 0.4	431.9 ± 4.5
	R4	17.4 ± 0.5	18.0 ± 0.5	411.8 ± 4.2
2019	V5	23.1 ± 0.1	23.4 ± 0.1	498.2 ± 5.8
	V6	25.6 ± 0.1	25.9 ± 0.1	476.0 ± 10.6
	V7	22.7 ± 0.1	23.0 ± 0.1	435.5 ± 8.1
	V8	20.4 ± 0.1	20.7 ± 0.1	496.2 ± 11.5
	V9	21.4 ± 0.1	21.9 ± 0.1	416.7 ± 7.7
	V10	21.8 ± 0.1	22.0 ± 0.1	517.5 ± 8.2
	V12	25.5 ± 0.1	25.7 ± 0.1	516.6 ± 6.9
	VT–R1	22.5 ± 0.1	22.8 ± 0.1	414.8 ± 5.1
	R2	23.2 ± 0.1	23.4 ± 0.0	423.2 ± 5.5
	R3	20.3 ± 0.1	20.5 ± 0.1	397.9 ± 4.7
	R4	19.2 ± 0.0	19.5 ± 0.0	163.4 ± 6.6
2020	V7	19.9 ± 0.1	20.2 ± 0.1	414.4 ± 8.6

Year	Growth stage	T_{min} (°C)	T_{max} (°C)	R_s (W m^{-2})
	V8	23.3 ± 0.1	23.6 ± 0.1	495.6 ± 5.6
	V9	22.8 ± 0.2	23.1 ± 0.2	523.3 ± 10.1
	V10	24.3 ± 0.1	24.6 ± 0.1	475.5 ± 8.0
	V12	23.7 ± 0.1	24.0 ± 0.1	467.2 ± 8.7
	VT–R1	23.7 ± 0.1	24.0 ± 0.1	408.7 ± 4.7
	R2	20.4 ± 0.1	20.7 ± 0.1	473.8 ± 5.1
	R3	22.5 ± 0.1	22.8 ± 0.1	460.4 ± 6.9
	R4	23.2 ± 0.1	23.5 ± 0.1	448.4 ± 2.9

Notes: Maize growth stages are abbreviated using the standard vegetative (V) and reproductive (R) staging system. Vegetative stages such as V5, V6, V7, V8, V9, V10, and V12 indicate the number of fully developed leaves with visible collars. VT–R1 represents the transition from tasseling to silking, when the tassel has fully emerged and silks begin to appear. R2 is the blister stage, when kernels are small and fluid filled. R3 is the milk stage, when kernels contain a milky inner fluid. R4 is the dough stage, when kernels begin to thicken and accumulate starch. Phenological growth-stage dates used in this study were obtained from field scouting records rather than estimated from a model.

3.2.3. Mechanistic Model Formulation

The available energy at the canopy scale is partitioned into sensible heat flux, latent heat flux, and heat storage (Jackson et al., 1981). This energy balance can be expressed as shown in Equation 3.3:

$$R_n = G + H + \lambda E \tag{3.3}$$

where R_n is net radiation (W m^{-2}), G is the canopy heat storage term (W m^{-2}), H is sensible heat flux from the canopy to the air (W m^{-2}), and λE is latent heat flux to the air (W m^{-2}), where λ represents the heat of vaporization. H and λE can be defined as shown in Equations 3.4 and 3.5, respectively:

$$H = \frac{\rho C_p (T_c - T_a)}{r_a} \tag{3.4}$$

$$\lambda E = \frac{\rho C_p (e_c^* - e_a)}{[\gamma (r_a + r_c)]} \tag{3.5}$$

where ρ is air density (kg m^{-3}), C_p is the specific heat capacity of air (J kg^{-1} K^{-1}), T_c is canopy temperature (°C), T_a is air temperature (°C), r_a is aerodynamic resistance to heat transfer (s m^{-1}), e_c^* is saturation vapor pressure at canopy temperature (kPa), e_a is ambient vapor pressure (kPa), γ

is the psychrometric constant (kPa K^{-1}), and r_c is canopy resistance (s m^{-1}). In this study, the non-water-stressed canopy temperature was denoted by $T_{c,ns}$.

To represent transient canopy heating and cooling, the canopy was treated as a lumped thermal system with a finite heat capacity. In this formulation, the canopy is represented as a single effective heat-storage unit with one representative canopy temperature and one effective heat capacity (C). Therefore, the heat storage term was expressed as:

$$G = C\frac{dT_c}{dt} \tag{3.6}$$

$$C = \rho^* {C_p}^* l^* \tag{3.7}$$

where C is the effective canopy heat capacity per unit ground area (J m^{-2} K^{-1}), representing the thermal inertia of the canopy as given in Equation 3.7, ρ^* is the effective canopy density, ${C_p}^*$ is the effective specific heat capacity of canopy, and l^* is the effective canopy depth. The term $\frac{dT_c}{dt}$ represents the temporal rate of change of canopy temperature. Rearranging Equation 3.3 to make G the subject and substituting Equations 3.4–3.6 gives the dynamic canopy-temperature equation shown in Equation 3.8:

$$C\frac{dT_c}{dt} = R_n - \frac{\rho C_p(T_c - T_a)}{r_a} - \frac{\rho C_p({e_c}^* - e_a)}{[\gamma(r_a + r_c)]} \tag{3.8}$$

Dividing Equation 3.8 by C yields a dynamic model that expresses canopy temperature as a function of R_n, T_a, and VPD as shown in Equation 3.9. This formulation is equivalent to the dynamic model described by Jones (2014), under the assumption that wind speed (u, m s^{-1}) has minimal influence on T_c or is implicitly represented through the aerodynamic resistance term.

The resulting model is a first-order differential equation in which multiple forcing inputs act on the plant system to produce a single T_c response, consistent with a multiple-input single-output system (Al-Faraj et al., 2000). In Equation 3.9, t is time, $\tau_{(a,r,v)}$ are the advective time delays associated with the T_a, radiation, and VPD forcing inputs, respectively:

$$\frac{dT_c(t)}{dt} + \frac{\rho C_p T_c(t)}{C r_a} = \frac{\rho C_p T_a(t-\tau_a)}{C r_a} + \frac{1}{C} \cdot R_n(t-\tau_r) - \frac{\rho C_p}{[C\gamma(r_a+r_c)]} \cdot (e_c{}^* - e_a)(t-\tau_v) \quad (3.9)$$

Equation 3.9 can be expressed in terms of VPD because the vapor pressure difference between the canopy and the surrounding air can be related to the atmospheric VPD (Adeyemi et al., 2018). The relationship is shown in Equation 3.10:

$$e_c{}^* - e_a = VPD + \Delta(T_c - T_a) \quad (3.10)$$

where Δ is the slope of the saturation-vapor-pressure curve with respect to temperature and is assumed to be approximately constant over the range from T_c to T_a (Jones, 2014). Defining $s = {}^{d}/_{dt}$ as the time-derivative operator and setting $a = \frac{\rho C_p}{C r_a}$, $b = \frac{1}{C}$, and $c = \frac{\rho C_p}{[C\gamma(r_a+r_c)]}$, Equation 3.9 can be transformed into the Laplace domain. Taking the Laplace transform of Equation 3.9, while accounting for the input-specific time delays, gives the compact dynamic expression shown in Equation 3.11.

$$(s+a)T_{c,ns}(t) = aT_a(t-\tau_a) + bR_n(t-\tau_r) - cVPD\ (t-\tau_v) \quad (3.11)$$

Cannavo et al. (2016) reported that, during the day, the net radiation above the canopy is almost equal to the total shortwave irradiance (R_s, W m^{-2}) when net radiation is measured above the crop and radiation exchange between the canopy and the ground is small; therefore, solar radiation was used in place of net radiation. Because Δ is approximately constant and VPD is treated as a time-varying input, Equation 3.11 can be expressed as a first-order continuous-time multiple input single-output (MISO) transfer function model, as shown in Equation 3.12. The resulting MISO function is equivalent to the model described and used by Adeyemi et al. (2018) to predict baseline temperature in greenhouse lettuce.

$$T_{c,ns}(t) = \frac{a}{s+a} T_a(t-\tau_a) + \frac{b}{s+a} R_s(t-\tau_r) - \frac{c}{s+a} VPD\ (t-\tau_v) \quad (3.12)$$

3.2.4. Data-Based Mechanistic Modeling Approach, Implementation, and Parameter Estimation

The mechanistic formulation developed in Section 3.2.3 showed that, under the assumptions of minimal wind effects and approximately constant Δ over the range of canopy and air temperatures, T_c can be represented as a first-order continuous-time dynamic system driven by T_a, R_s, and VPD. This led to the transfer-function representation in Equation 3.12. To estimate these quantities from measured data, a data-based mechanistic (DBM) modeling approach was adopted. In the DBM framework, physical knowledge of the system is first used to formulate a mechanistic model structure, after which time-series input-output data are used to estimate the unknown parameters and delays. This framework consists of a mechanistic phase and a data-based phase, and has been described by Young (2006) and Desta et al. (2004), and applied by Adeyemi et al. (2018) in a related canopy temperature modeling study. Following the DBM representation of the transfer systems, Equation 3.12 can be written in a general continuous-time multiple-input, single-output (MISO) form shown in Equation 3.13:

$$z(t) = \sum_{k=1}^{K} \frac{B_k(s)}{A(s)} u_k(t - \delta_k) + \frac{1}{W(s)} e(t) \tag{3.13}$$

where $z(t)$ denotes the output, which in this study is the non-water-stressed canopy temperature $T_{c,ns}(t)$; $u_k(t)$ denotes the set of input variables $\{T_a, R_s, VPD\}$; δ_k represents the advective time delay associated with each input; and $e(t)$ is the stochastic disturbance term. The transfer function was written in terms of the derivative operator $s = d/dt$, with denominator and numerator polynomials given in Equations 3.14 and 3.15, respectively:

$$A(s) = s^n + z_1 s^{n-1} + \cdots + z_{n-1} s + z_n \tag{3.14}$$

$$B(s) = x_0 s^m + x_1 s^{m-1} + \cdots + x_{m-1} s + x_m \tag{3.15}$$

Thus, the general model structure was defined by the triad $[n, m, \delta]$, where n is the denominator order, m is, the order of each numerator polynomial, and δ denotes the input-specific delay. By comparing Equation 3.12 with Equation 3.13, this study adopted a first-order denominator $(n = 1)$ and first-order numerators $(m = 1)$, such that the parameters to be identified were a, b, and c, and the delays τ_a, τ_r, and τ_v. This formulation provided a physically interpretable representation of maize canopy temperature dynamics suitable for continuous-time identification.

Model implementation followed the workflow summarized in Figure 3.1 and was carried out in two stages: data preprocessing in R version 4.5.2 (R Core Team, 2025) and model delay and parameter identification in MATLAB using the CAPTAIN toolbox. Prior to model estimation, T_c data from FIT, representing non-water-stressed conditions, together with T_a and R_s, were filtered and cleaned. VPD was computed from the one-minute meteorological observations, and the resulting dataset containing T_c, T_a, R_s, and VPD was restricted to observations collected between 12:30 and 16:30 standard local time, corresponding to the period of strongest canopy–atmosphere coupling. The filtered observations were then stratified by maize growth stage for each growing season and aggregated into minute-of-day averages within each stage. Specifically, observations recorded at the same clock minute were averaged across all dates assigned to each year–stage combination, producing one stage-specific mean diurnal profile for T_c and each meteorological input. This preprocessing reduced short-term and between-day variability while preserving the dominant within-afternoon T_c response used for model identification. The resulting profiles therefore represent stage-averaged, rather than individual daily, non-water-stressed canopy-temperature trajectories. This procedure assumes that canopy–atmosphere dynamics are approximately stationary within each phenological stage but may change between stages. Adeyemi

et al. (2018) applied a similar piecewise-stationary approach using leaf area index intervals; in the present study, segmentation was based on maize phenological growth stages.

After preprocessing, an interannual dynamic transferability framework was implemented, whereby data from one growing season were used for parameter and delay identification and data from another growing season were used for independent testing, considering only growth stages common to both years. Parameter identification was carried out in MATLAB using the CAPTAIN toolbox and the recursive refined instrumental variable (RIVC) algorithm for continuous-time systems. In this workflow, both the delays and the model parameters were identified from the training data. The delays associated with air temperature (τ_a), $R_s(\tau_r)$, and VPD (τ_v) were identified using a discrete RIVC-based local search procedure. Because the stage-specific time series were represented at a 1-min temporal resolution, each candidate delay corresponded to an integer-minute lag applied to the corresponding input variable, such that the model used $T_a(t - \tau_a)$, $R_s(t - \tau_r)$, and $VPD(t - \tau_v)$. For each candidate delay combination, the first-order continuous-time MISO model was fitted using RIVC, and candidate models were compared using prediction error, residual diagnostics, and consistency with physically expected parameter signs. The selected delay combination was the one that minimized prediction error while maintaining physically realistic parameter estimates and acceptable residual behavior. After the delay structure was selected, the final model parameters a, b, and c were estimated using RIVC for each growth-stage-specific training dataset. Predictive performance was quantified using the coefficient of determination (R^2), mean absolute error (MAE), and root mean square error (RMSE), as defined in Equations 3.16, 3.17, and 3.18, respectively.

$$R^2 = 1 - \frac{\sum_{i=1}^{n}(y_i - \hat{y}_i)^2}{\sum_{i=1}^{n}(y_i - \bar{y})^2} \tag{3.16}$$

$$MAE = \frac{1}{n}\sum_{i=1}^{n}|y_i - \hat{y}_i| \tag{3.17}$$

$$RMSE = \sqrt{\frac{1}{n}\sum_{i=1}^{n}(y_i - \hat{y}_i)^2} \tag{3.18}$$

where y_i is the observed canopy temperature, $\hat{y}_i$ is the model predicted canopy temperature, $\bar{y}$ is the mean of the observed canopy temperature, and n is the number of observations.

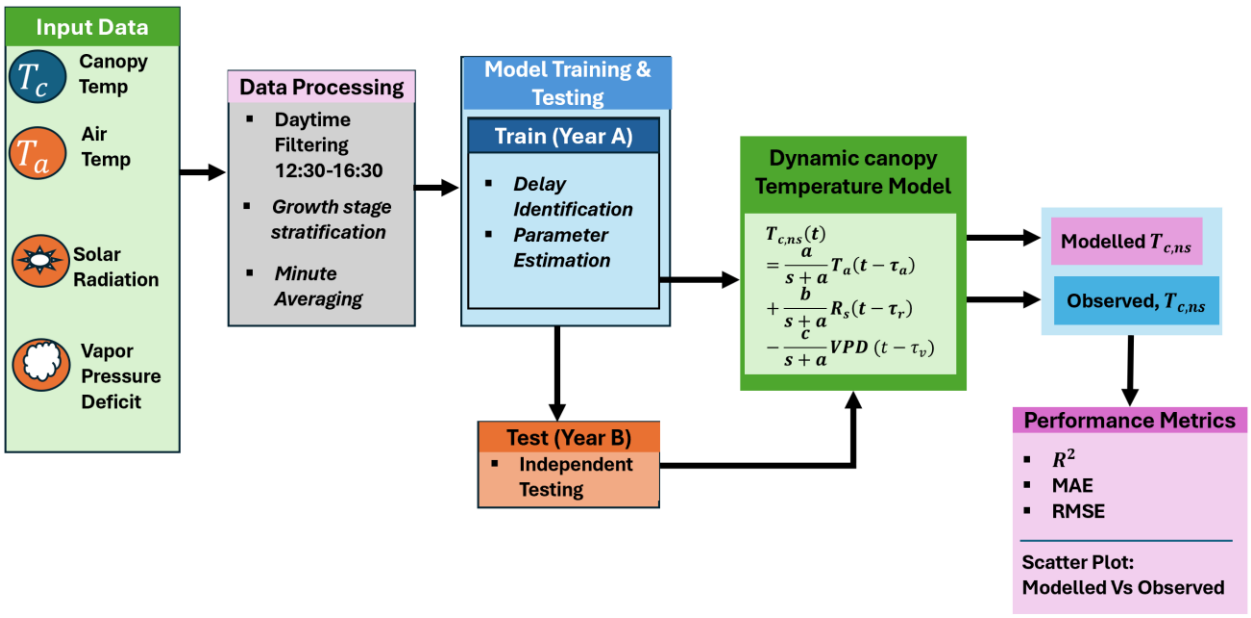


Figure 3.1. Data-based mechanistic modeling framework used for identification and evaluation of the maize canopy temperature model. Input data ($\boldsymbol{T_c}$, $\boldsymbol{T_a}$, $\boldsymbol{R_s}$, and VPD) were filtered to the 12:30–16:30 period, stratified by growth stage, and aggregated into minute-of-day averages before model training and independent cross-year testing. During training, input delays and model parameters were identified for the first-order dynamic canopy temperature model, and predictive performance on the test year was assessed using $\boldsymbol{R^2}$, MAE, and RMSE.

3.3. Results and Discussion

3.3.1. Cross-Year Predictive Performance of the DBM Model

The first-order continuous-time transfer function driven by air temperature, R_s, and VPD reproduced the observed diurnal trajectory of $T_{c,ns}$ across independent growing seasons in field-grown maize. Performance varied systematically by phenological stage rather than by the direction of cross-year transfer. Across all train–test combinations (Table 3.2), MAE ranged from 0.093 to 0.442 °C, RMSE ranged from 0.122 to 0.838 °C, and test R^2 ranged from 0.391 to 0.958. Training on 2018 and testing on 2020 produced the strongest overall performance at R4, with the lowest MAE (0.093 °C), the lowest RMSE (0.122 °C), and the highest R^2 (0.958). Strong performance was also observed at R3: training on 2019 and testing on 2020 yielded an MAE of 0.167 °C and R^2 of 0.958, whereas training on 2020 and testing on 2018 yielded an MAE of 0.179 °C, RMSE of 0.229 °C, and R^2 of 0.742. At VT–R1, both evaluations yielded an MAE of 0.216 °C, with R^2 ranging from 0.709 to 0.756. The weakest performance occurred when the model was trained on 2020 and tested on 2019 at V8 and V9. V8 had the highest MAE (0.442 °C; RMSE = 0.556 °C; $R^2 = 0.503$), whereas V9 had the highest RMSE (0.838 °C; MAE = 0.408 °C; $R^2 = 0.397$). Performance at R2 was also comparatively weak when the model trained on 2019 was evaluated on 2018 or 2020, with MAE ranging from 0.250 to 0.275 °C and R^2 remaining near 0.39. The observed and modeled $T_{c,ns}$ series in Figure 3.2 show that the model reproduced the dominant diurnal rise and midafternoon plateau at the better-performing stages but exhibited larger phase and amplitude discrepancies at V8, V9, and R2.

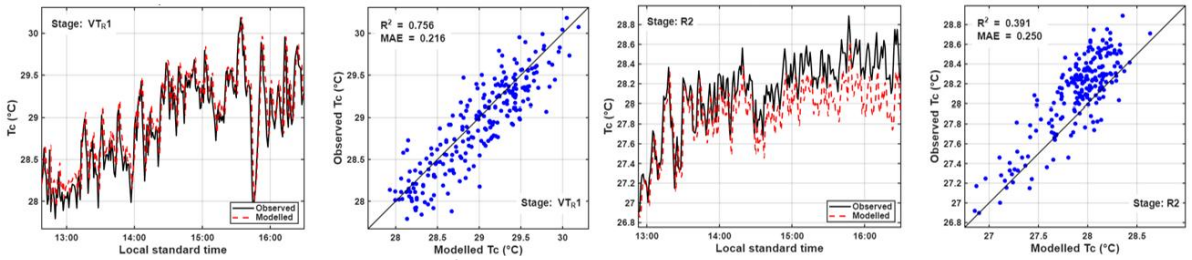
Table 3.2. Interannual dynamic transferability performance of the DBM model for predicting $\mathbf{T_{c,ns}}$ across maize growth stages, expressed as $\boldsymbol{R^2}$, MAE (°C), and RMSE (°C).

Training year	Testing year	Stage	Test R^2	MAE (°C)	RMSE (°C)
2018	2020	R4	0.958	0.093	0.122
2019	2020	V10	0.565	0.344	0.401
		VT–R1	0.709	0.216	0.289
		R2	0.391	0.275	0.386
		R3	0.958	0.167	0.218
	2018	VT–R1	0.756	0.216	0.270
		R2	0.391	0.250	0.300
2020	2019	V8	0.503	0.442	0.556
		V9	0.397	0.408	0.838
		V10	0.867	0.202	0.250
		R3	0.686	0.342	0.413
		R4	0.707	0.306	0.354
	2018	R3	0.742	0.179	0.229

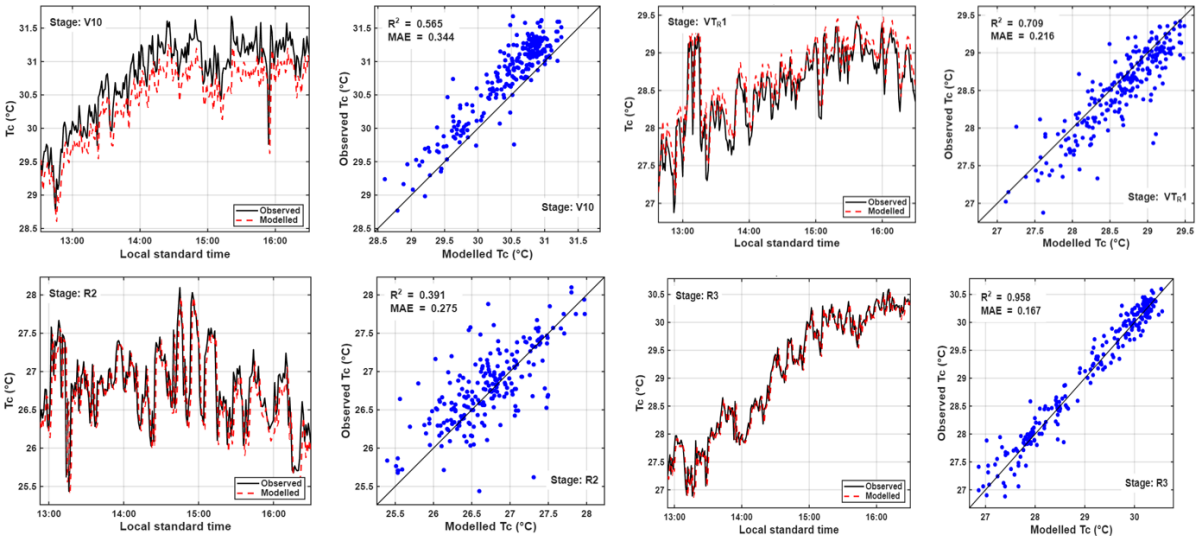
These findings demonstrate cross-year transferability rather than in-sample fit because parameters identified from one growing season were applied without modification to an independent season with different meteorological forcing. Young (2006) described this as a core strength of data-based mechanistic analysis: embedding physical knowledge in the transfer-function structure can identify dynamics that persist under changing conditions rather than only contemporaneous statistical relationships. Adeyemi et al. (2018) applied a DBM approach to greenhouse-grown lettuce and reported MAE values of 0.17–0.29 °C and RMSE values of 0.21–0.35 °C. Those values compare favorably with the MAE of 0.167–0.179 °C at R3 and 0.093 °C at R4 in this study, despite the greater variability in radiation, VPD, wind, and canopy development under field conditions. This comparison indicates that DBM prediction of baseline temperatures can extend from regulated environments to field-grown crops during phonologically stable stages.

Using multiple linear regression, Payero et al. (2005a) reported $T_{c,ns}$ prediction coefficients of determination of 0.89–0.94 for alfalfa and tall fescue, while Nakabuye et al. (2024) reported a pooled coefficient of determination of 0.94 for field-grown maize under semiarid conditions. King and Shellie (2016) reported MAE values of 0.82–0.98 °C when neural networks were used to predict non-water-stressed wine-grape leaf temperature from meteorological inputs. The lower errors obtained at the strongest stages in this study suggest that the physical constraints of the first-order transfer-function structure extracted predictive information efficiently from limited training data, consistent with the parsimony argument of Taylor et al. (2007).

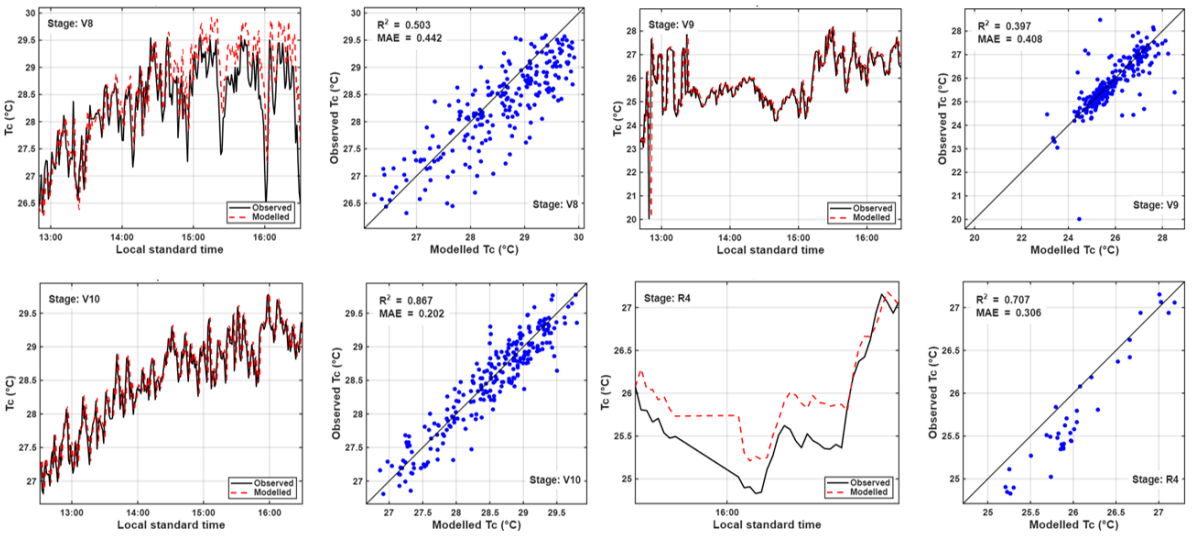
A) Train 2019 → Test 2018



B) Train 2019 → Test 2020



C) Train 2020 → Test 2019



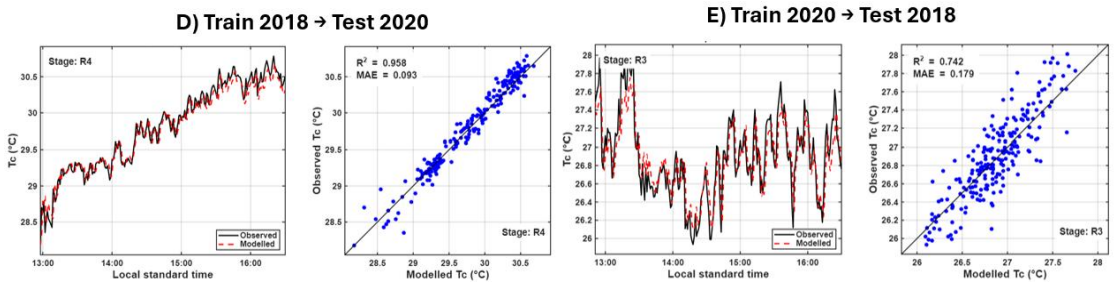


Figure 3.2. Stage-specific cross-year predictive performance of the DBM canopy temperature ($\boldsymbol{T_c}$) model. In each panel, observed and modeled $\boldsymbol{T_c}$ are compared using time-series plots and observed-versus-modeled scatter plots. Panel A corresponds to training on 2019 and testing on 2018, Panel B to training on 2019 and testing on 2020, Panel C to training on 2020 and testing on 2019, Panel D to training on 2018 and testing on 2020, and Panel E to training on 2020 and testing on 2018. The accompanying $\boldsymbol{R^2}$ and MAE statistics quantify goodness-of-fit and prediction error, respectively, for each maize growth stage under independent validation. Here, VT–R1 denotes the combined tasseling-to-silking stage.

3.3.2. Error Structure and Stage-Specific Model Behavior

The prediction-error distributions in Figure 3.3 provide additional insight into the growth-stage dependence of model performance. At R3 and R4, where cross-year MAE was lowest, the violin plots were compact, approximately symmetric, and centered near zero, indicating small errors and little directional bias. At V8 and V9, the distributions were wider and had extended tails in both directions, showing greater within-stage variability. R2 exhibited a different pattern: a positive mean error indicated systematic underestimation of $T_{c,ns}$, with direct implications for CWSI calculation, as discussed in Section 3.3.3. The error structure can also be considered alongside the parameter estimates in Table A.1. At R3, where MAE remained comparatively low across evaluations, the parameter estimates identified from the 2020 training season were large relative to their standard errors. For the 2020-to-2019 and 2020-to-2018 evaluations, a ranged from 0.356 to 0.369, b from 0.226 to 0.268, and c from 0.404 to 0.449, with all associated standard errors below 0.10. The moderate value of a at R3 is consistent with aerodynamic coupling between

the closed canopy and the atmosphere in the energy-balance formulation of Jones (2014), where a represents the ratio of aerodynamic heat-transport capacity to effective canopy heat capacity.

The consistently positive values of c across stages indicate that higher atmospheric VPD was associated with lower $T_{c,ns}$, as expected when increasing atmospheric demand enhances latent heat dissipation and evaporative cooling in a well-watered canopy (Idso et al., 1981; Jones, 1999). By contrast, the V9 parameter estimates had large relative standard errors, with the standard errors exceeding the corresponding estimates (b = 0.031 ± 0.233; c = 0.079 ± 0.239). Likewise, when the model was trained on 2020 and tested on 2019 at R4, the standard error of the VPD parameter was nearly equal to its estimate ($c = 0.691 \pm 0.660$), indicating limited estimation precision. Poor parameter identifiability and high MAE therefore occurred together at stages where the stage-averaged diurnal profiles contained insufficient information to resolve all three parameters simultaneously, a recognized feature of ill-posed environmental system-identification problems. The performance gradient across growth stages can be related to changes in canopy architecture, aerodynamic behavior, and canopy–atmosphere coupling during maize development (Duan et al., 2024; Tian et al., 2024; Zhu et al., 2025). This interpretation is consistent with Liao et al. (2024), who showed that the maize non-water-stressed baseline varied with growth stage and genotype.

Mahan et al. (2015) showed that canopy-temperature responses to atmospheric demand are regulated by stage- and environment-dependent stomatal behavior, providing a physiological basis for the greater parameter variability observed during vegetative and early grain-fill stages. At V8 and V9, year-specific differences in leaf area, canopy height, and canopy cover may cause parameters identified in one season to represent another season poorly, consistent with the wide error distributions in Figure 3.3. The systematic positive bias at R2 may reflect an interannual mismatch in atmospheric forcing. As shown in Table 3.1, mean solar radiation during R2 in 2019

was lower than during the corresponding periods in other years, indicating a substantial difference between training and evaluation environments. If VPD or radiation loading during the training year was systematically higher than during the testing year, parameters calibrated under the more energetically demanding conditions would predict more strongly cooled $T_{c,ns}$ values, producing the positive bias in Figure 3.3. This mechanism is consistent with the model structure and supports interpreting the R2 bias as a meteorological-transfer problem rather than solely as structural model failure. Liao et al. (2024) attributed interannual sensitivity of the maize non-water-stressed baseline during silking to genotype-by-environment interactions, while Mahan et al. (2015) noted that stomatal regulation during early grain fill is sensitive to prior VPD conditions. Both mechanisms could amplify interannual parameter divergence at R2. The longer delays identified at R2 (Table A.2) further suggest a distributed and inertially complex response that the present first-order formulation may not fully capture under cross-year transfer.

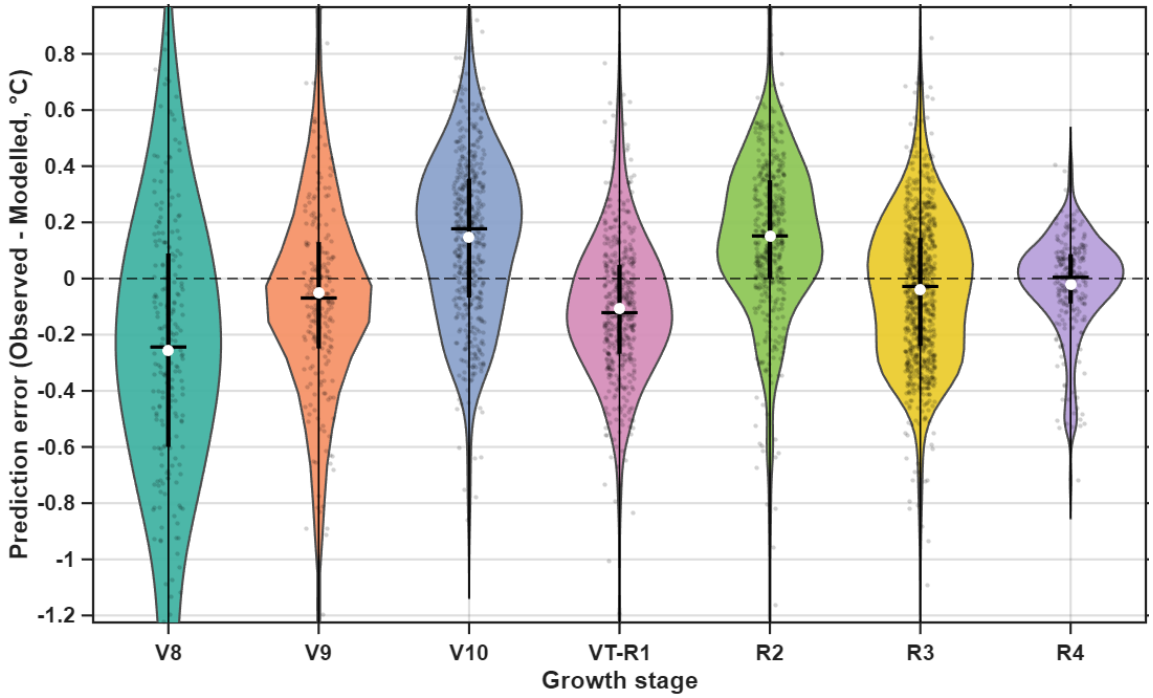


Figure 3.3. Distribution of model prediction errors across maize growth stages (V8–R4). Violin plots represent the density of errors for each stage, with overlaid points showing individual

observations. The white markers indicate mean prediction error, and the horizontal bars represent variability around the mean. The dashed horizontal line at zero denotes perfect model agreement, where positive values indicate underestimation and negative values indicate overestimation by the model.

3.3.3. Implications for Empirical CWSI Estimation and Irrigation Water Management

The results of this study have direct implications for the use of modeled $T_{c,ns}$ as the lower baseline in empirical CWSI computation for maize grown under semi-arid conditions. The strong cross-year performance achieved at R3 and R4 shows that a DBM framework can provide reliable estimates of $T_{c,ns}$ during key reproductive stages without requiring continuous maintenance of a dedicated non-water-stressed reference treatment in the prediction year. This is practically important because one of the major limitations of empirical CWSI approaches has long been the difficulty of obtaining robust lower-baseline temperatures under field conditions throughout the season (Katimbo et al., 2022; Nakabuye et al., 2024; Wanjura et al., 2003). By demonstrating that $T_{c,ns}$ can be predicted dynamically from standard weather inputs with relatively small error during the most transferable stages, the present study supports the feasibility of replacing direct reference-based baseline determination with a stage-specific predictive framework that remains physically interpretable and operationally more flexible. These findings are especially relevant for irrigation scheduling because the model performed best during the later reproductive period, when maize is highly sensitive to water deficits and accurate stress detection is most critical for protecting yield. Previous studies have shown that canopy temperature-based stress indices can be effective for irrigation timing in maize and that the early- to mid-afternoon period is often the most informative window for detecting stress-related thermal divergence among treatments (Irmak et al., 2000; Nakabuye et al., 2022; Taghvaeian, Chávez, et al., 2014). The present results are consistent with

that literature and extend it by showing that the lower reference temperature needed for empirical CWSI can itself be treated as a dynamic, stage-dependent variable rather than as a purely static regression quantity or a value that must always be measured directly. At R3 and R4, the observed MAE values were small relative to the canopy-temperature-based irrigation thresholds for maize reported in the literature. For example, Nakabuye et al. (2022) reported that a degrees above non-stressed (DANS) threshold of 0.5 °C was suitable for triggering irrigation in maize under semi-arid conditions. Across all cross-year evaluations at R3 and R4, MAE ranged from 0.093 to 0.342 °C, below this 0.5 °C threshold.

At the same time, the weaker transfer at V8, V9, and R2 indicates that dynamic prediction of $T_{c,ns}$ is not yet equally robust across the whole maize season, and this should be treated as an important operational boundary for this framework. In those stages, the higher error and, in the case of R2, the positive bias would propagate into CWSI in ways that could alter irrigation decisions if used without recalibration. The most defensible interpretation, therefore, is not that the model provides a universally stable lower baseline temperature, but that it identifies where dynamic baseline prediction is currently most credible and where additional refinement is still needed. In practice, this means that cross-year DBM-based estimation of $T_{c,ns}$ appears most promising for later reproductive stages, whereas earlier vegetative and transitional stages may require in-season updating. Framed in this way, the study contributes both scientifically and operationally: it shows that dynamic lower-baseline prediction is feasible in field maize, clarifies the phenological windows in which it is most defensible, and provides a realistic pathway toward more automated, plant-centered irrigation scheduling in water-limited environments.

3.4. Conclusions

This study developed and evaluated a data-based mechanistic dynamic modeling framework for predicting non-water-stressed canopy temperature in field-grown maize under semiarid conditions and assessed its performance across growth stages. The framework represented $T_{c,ns}$ as a first-order continuous-time dynamic system driven by air temperature, R_s, and vapor pressure deficit. Parameters identified in one growing season were transferred without modification to independent seasons under different meteorological forcing, demonstrating the potential of the framework as a physically grounded alternative to static regression and reference-surface approaches for $T_{c,ns}$ estimation. Predictive performance nevertheless varied systematically with phenological stage. Transferability was strongest during the late reproductive stages, when full canopy closure produced a more stable canopy–atmosphere coupling environment, and weakest at the mid-vegetative stages and R2, where changing canopy architecture and interannual meteorological variability limited transfer. This stage dependence confirms that the dynamics governing non-water-stressed maize canopy temperature are not seasonally invariant and that growth-stage-specific parameterization is necessary when the framework is applied across the season.

Several limitations should be recognized. The cross-year evaluation was conducted at one semi-arid Nebraska site over three growing seasons, so the generalizability of the parameter sets and stage-specific performance patterns to other environments, genotypes, and production systems remains to be established. The model assumed minimal wind effects and therefore excluded wind speed as an explicit input; this simplification may have contributed to higher errors at vegetative stages, when a partially open canopy is more sensitive to aerodynamic coupling. The stage-averaged diurnal profiles also aggregate temporal variation and may not fully represent within-

stage dynamics during rapid canopy development. In addition, the model was trained only with data from the fully irrigated treatment and was not evaluated for partially stressed canopies. Despite these limitations, the results demonstrate that a physically interpretable dynamic framework can predict non-water-stressed canopy temperature in field-grown maize with accuracy competitive with published regression and machine-learning approaches while also characterizing stage-dependent temporal responses. Future work should evaluate the framework across sites and genotypes, incorporate wind speed and canopy structure, and test recursive in-season recalibration to extend reliable prediction across the maize season. These steps would support the transition from experimental demonstration to operational, plant-centered irrigation scheduling in water-limited environments.

Chapter 4 - Summary and Conclusions

4.1. Conclusions

The first objective was to identify suitable growth-stage-specific measurement periods for developing soybean non-water-stressed baselines and to derive the corresponding baselines. Measurement timing directly affected the reference used to interpret canopy temperature: selected periods shifted from mid-to-late afternoon during vegetative development to solar noon or early afternoon during reproductive development. Relative to these periods, the conventional 14:00–15:00 h interval increased posterior mean RMSE by 3.3–43.0%. Baseline slopes and intercepts also differed among growth stages. These results show that one fixed measurement period and one seasonal baseline may not adequately represent non-water-stressed soybean canopy behavior throughout development. Accounting for growth stage can reduce avoidable error in CWSI estimation and strengthen its relationship with crop response.

The second objective was to develop and evaluate a dynamic data-based mechanistic model for predicting non-water-stressed maize canopy temperature from air temperature, solar radiation, and vapor pressure deficit. Parameters identified in one season were applied without modification to independent seasons, demonstrating that the reference temperature can be predicted from routinely measured weather variables without continuous measurements from a fully irrigated reference crop. Performance remained growth-stage dependent: across all evaluations, mean absolute error ranged from 0.093 to 0.442 °C and the coefficient of determination ranged from 0.391 to 0.958. At the milk and dough stages, the MAE ranged from 0.093 to 0.342 °C and the coefficient of determination ranged from 0.686 to 0.958, whereas performance was weaker at V8, V9, and the blister stage.

The central contribution of this thesis is a growth-stage-aware framework for improving CWSI estimation. Stage-specific selection of canopy-temperature observations can strengthen empirical baseline development, while dynamic prediction can reduce dependence on continuously maintained well-watered reference treatments. Together, the approaches can improve seasonal consistency, reduce the land, water, instrumentation, and management required to obtain reference temperatures, and support more automated crop water-stress monitoring. The broader conclusion is that the non-water-stressed thermal reference should be treated as a dynamic, development-dependent quantity rather than a fixed seasonal value.

4.2. Future Work

Future work should validate the selected measurement periods and dynamic model across additional locations, seasons, cultivars, and management conditions. Measurement periods should be evaluated relative to local solar time, and the dynamic model should be tested with wind speed and canopy characteristics such as leaf area index, canopy cover, and crop height. The measured and predicted reference temperatures should then be incorporated into real-time CWSI calculations and evaluated in irrigation-scheduling experiments to determine whether they improve stress detection, conserve irrigation water, maintain yield, and support practical automation.

References

Abdul-Jabbar, A. S., Lugg, D. G., Sammis, T. W., & Gay, L. W. (1985). Relationships between crop water stress index and alfalfa yield and evapotranspiration. *Transactions of the ASAE*, *28*(2), 454–461. https://doi.org/10.13031/2013.32278

Adeyemi, O., Grove, I., Peets, S., Domun, Y., & Norton, T. (2018). Dynamic modelling of the baseline temperatures for computation of the crop water stress index (CWSI) of a greenhouse cultivated lettuce crop. *Computers and Electronics in Agriculture*, *153*, 102–114. https://doi.org/10.1016/j.compag.2018.08.009

Alderfasi, A. A., & Nielsen, D. C. (2001). Use of crop water stress index for monitoring water status and scheduling irrigation in wheat. *Agricultural Water Management*, *47*(1), 69–75. https://doi.org/10.1016/S0378-3774(00)00096-2

Al-Faraj, A., Meyer, G. E., Schade, G. R., & Horst, G. L. (2000). Dynamic analysis of moisture stress in tall fescue (*Festuca arundinacea*) using canopy temperature, irradiation, and vapor deficit. *Transactions of the ASAE*, *43*(1), 101–109. https://doi.org/10.13031/2013.2674

Allen, R. G., Pereira, L. S., Raes, D., & Smith, M. (1998). Crop evapotranspiration: Guidelines for computing crop water requirements (FAO Irrigation and Drainage Paper No. 56). Food and Agriculture Organization of the United Nations.

Allen, R. G., Walter, I. A., Elliott, R. L., Howell, T. A., Itenfisu, D., Jensen, M. E., & Snyder, R. L. (2005). The ASCE standardized reference evapotranspiration equation. American Society of Civil Engineers. https://doi.org/10.1061/9780784408056

Apolo-Apolo, O. E., Martínez-Guanter, J., Pérez-Ruiz, M., & Egea, G. (2020). Design and assessment of new artificial reference surfaces for real time monitoring of crop water stress index in maize. *Agricultural Water Management*, *240*, 106304. https://doi.org/10.1016/j.agwat.2020.106304

Ashley, D. A., & Ethridge, W. J. (1978). Irrigation effects on vegetative and reproductive development of three soybean cultivars. *Agronomy Journal*, *70*(3), 467–471. https://doi.org/10.2134/agronj1978.00021962007000030026x

Baker, J. T., Mahan, J. R., Gitz, D. C., Lascano, R. J., & Ephrath, J. E. (2013). Comparison of deficit irrigation scheduling methods that use canopy temperature measurements. *Plant Biosystems - An International Journal Dealing with All Aspects of Plant Biology*, *147*(1), 40–49. https://doi.org/10.1080/11263504.2012.736423

Blad, B. L., & Baker, D. G. (1972). Orientation and distribution of leaves within soybean canopies. *Agronomy Journal*, *64*(1), 26–29. https://doi.org/10.2134/agronj1972.00021962006400010009x

Bockhold, D. L., Thompson, A. L., Sudduth, K. A., & Henggeler, J. C. (2011). Irrigation scheduling based on crop canopy temperature for humid environments. *Transactions of the ASABE*, *54*(6), 2021–2028. https://doi.org/10.13031/2013.40654

Campbell, G. S., & Norman, J. M. (2000). *An introduction to environmental biophysics (2nd ed.)*. Springer.

Candogan, B. N., Sincik, M., Buyukcangaz, H., Demirtas, C., Goksoy, A. T., & Yazgan, S. (2013). Yield, quality and crop water stress index relationships for deficit-irrigated soybean [G*lycine max* (L.) Merr.] in sub-humid climatic conditions. *Agricultural Water Management*, *118*, 113–121. https://doi.org/10.1016/j.agwat.2012.11.021

Cannavo, P., Bouhoun Ali, H., Chantoiseau, E., Migeon, C., Charpentier, S., & Bournet, P.-E. (2016). Stomatal resistance of New Guinea *Impatiens* pot plants. Part 2: Model extension for water restriction and application to irrigation scheduling. *Biosystems Engineering*, *149*, 82–93. https://doi.org/10.1016/j.biosystemseng.2016.07.001

Clawson, K. L., Jackson, R. D., & Pinter, P. J., Jr. (1989). Evaluating plant water stress with canopy temperature differences. Agronomy Journal, 81(6), 858–863. https://doi.org/10.2134/agronj1989.00021962008100060004x

Cressie, N., & Wikle, C. K. (2011). *Statistics for spatio-temporal data*. John Wiley & Sons.

DeJonge, K. C., Taghvaeian, S., Trout, T. J., & Comas, L. H. (2015). Comparison of canopy temperature-based water stress indices for maize. *Agricultural Water Management*, *156*, 51–62. https://doi.org/10.1016/j.agwat.2015.03.023

Desta, T. Z., Van Brecht, A., Meyers, J., Baelmans, M., & Berckmans, D. (2004). Combining CFD and data-based mechanistic (DBM) modelling approaches. *Energy and Buildings*, *36*(6), 535–542. https://doi.org/10.1016/j.enbuild.2003.12.015

Dogan, E., Kirnak, H., & Copur, O. (2007). Deficit irrigations during soybean reproductive stages and CROPGRO-soybean simulations under semi-arid climatic conditions. *Field Crops Research*, *103*(2), 154–159. https://doi.org/10.1016/j.fcr.2007.05.009

Doss, B. D., Pearson, R. W., & Rogers, H. T. (1974). Effect of soil water stress at various growth stages on soybean yield. *Agronomy Journal*, *66*(2), 297–299. https://doi.org/10.2134/agronj1974.00021962006600020032x

Duan, M., Zhang, X., Wei, Z., Chen, X., & Zhang, B. (2024). Effect of maize canopy structure on light interception and radiation use efficiency at different canopy layers. *Agronomy*, *14*(7), 1511. https://doi.org/10.3390/agronomy14071511

Eck, H. V., Mathers, A. C., & Musick, J. T. (1987). Plant water stress at various growth stages and growth and yield of soybeans. *Field Crops Research*, *17*(1), 1–16. https://doi.org/10.1016/0378-4290(87)90077-3

Ekinzog, E. K., Schlerf, M., Kraft, M., Werner, F., Riedel, A., Rock, G., & Mallick, K. (2022). Revisiting crop water stress index based on potato field experiments in Northern Germany. *Agricultural Water Management*, *269*, 107664. https://doi.org/10.1016/j.agwat.2022.107664

Emekli, Y., Bastug, R., Buyuktas, D., & Emekli, N. Y. (2007). Evaluation of a crop water stress index for irrigation scheduling of bermudagrass. *Agricultural Water Management*, *90*(3), 205–212. https://doi.org/10.1016/j.agwat.2007.03.008

Fattahi, K., Babazadeh, H., Najafi, P., & Sedghi, H. (2018). Scheduling maize irrigation based on crop water stress index (CWSI). *Applied Ecology and Environmental Research*, *16*(6), 7535–7549. https://doi.org/10.15666/aeer/1606_75357549

Foroud, N., Mündel, H.-H., Saindon, G., & Entz, T. (1993). Effect of level and timing of moisture stress on soybean plant development and yield components. *Irrigation Science*, *13*(4), 149–155. https://doi.org/10.1007/BF00190029

Gardner, B. R., Nielsen, D. C., & Shock, C. C. (1992). Infrared thermometry and the crop water stress index. II. Sampling procedures and interpretation. *Journal of Production Agriculture*, *5*(4), 466–475. https://doi.org/10.2134/jpa1992.0466

Geiser, K. M., Slack, D. C., Allred, E. R., & Stange, K. W. (1982). Irrigation scheduling using crop canopy-air temperature difference. *Transactions of the ASAE*, *25*(3), 689–694. https://doi.org/10.13031/2013.33595

Gelman, A., Carlin, J. B., Stern, H. S., Dunson, D. B., Vehtari, A., & Rubin, D. B. (2013). *Bayesian data analysis* (3rd ed.). Chapman and Hall/CRC. https://doi.org/10.1201/b16018

Grant, O. M., Tronina, Ł., Ramalho, J. C., Kurz Besson, C., Lobo-do-Vale, R., Santos Pereira, J., Jones, H. G., & Chaves, M. M. (2010). The impact of drought on leaf physiology of *Quercus suber* L. trees: Comparison of an extreme drought event with chronic rainfall reduction. *Journal of Experimental Botany*, *61*(15), 4361–4371. https://doi.org/10.1093/jxb/erq239

Grimes, D. W., Wiley, P. L., & Sheesley, W. R. (1992). Alfalfa yield and plant water relations with variable irrigation. *Crop Science*, *32*(6), 1381–1387. https://doi.org/10.2135/cropsci1992.0011183X003200060015x

Gu, S., Liao, Q., Gao, S., Kang, S., Du, T., & Ding, R. (2021). Crop water stress index as a proxy of phenotyping maize performance under combined water and salt stress. *Remote Sensing*, *13*(22), 4710. https://doi.org/10.3390/rs13224710

Han, M., Zhang, H., DeJonge, K. C., Comas, L. H., & Gleason, S. (2018). Comparison of three crop water stress index models with sap flow measurements in maize. *Agricultural Water Management*, *203*, 366–375. https://doi.org/10.1016/j.agwat.2018.02.030

Hatfield, J. L., & Prueger, J. H. (2015). Temperature extremes: Effect on plant growth and development. *Weather and Climate Extremes, 10*, 4–10. https://doi.org/10.1016/j.wace.2015.08.001

Hattendorf, M. J., Carlson, R. E., Halim, R. A., & Buxton, D. R. (1988). Crop water stress index and yield of water-deficit-stressed alfalfa. *Agronomy Journal*, *80*(6), 871–875. https://doi.org/10.2134/agronj1988.00021962008000060006x

Heatherly, L. G. (1983). Response of soybean cultivars to irrigation of a clay soil. *Agronomy Journal*, *75*(6), 859–864. https://doi.org/10.2134/agronj1983.00021962007500060004x

Hernandez, C. M., Correndo, A., Kyveryga, P., Prestholt, A., & Ciampitti, I. A. (2023). On-farm soybean seed protein and oil prediction using satellite data. *Computers and Electronics in Agriculture*, *212*, 108096. https://doi.org/10.1016/j.compag.2023.108096

Hou, M., Tian, F., Zhang, T., & Huang, M. (2019). Evaluation of canopy temperature depression, transpiration, and canopy greenness in relation to yield of soybean at reproductive stage based on remote sensing imagery. *Agricultural Water Management*, *222*, 182–192. https://doi.org/10.1016/j.agwat.2019.06.005

Idso, S. B. (1982). Non-water-stressed baselines: A key to measuring and interpreting plant water stress. *Agricultural Meteorology*, *27*(1), 59–70. https://doi.org/10.1016/0002-1571(82)90020-6

Idso, S. B., Jackson, R. D., Pinter, P. J., Reginato, R. J., & Hatfield, J. L. (1981). Normalizing the stress-degree-day parameter for environmental variability. *Agricultural Meteorology*, *24*, 45–55. https://doi.org/10.1016/0002-1571(81)90032-7

Idso, S. B., Pinter, P. J., & Reginato, R. J. (1990). Non-water-stressed baselines: The importance of site selection for air temperature and air vapour pressure deficit measurements. *Agricultural and Forest Meteorology*, *53*(1), 73–80. https://doi.org/10.1016/0168-1923(90)90125-P

Irmak, S., Haman, D. Z., & Bastug, R. (2000). Determination of crop water stress index for irrigation timing and yield estimation of corn. *Agronomy Journal*, *92*(6), 1221–1227. https://doi.org/10.2134/agronj2000.9261221x

Irmak, S., Specht, J. E., Odhiambo, L. O., Rees, J. M., & Cassman, K. G. (2014). Soybean yield, evapotranspiration, water productivity, and soil water extraction response to subsurface drip irrigation and fertigation. *Transactions of the ASABE, 57*(3), 729–748. https://doi.org/10.13031/trans.57.10085

Jackson, R. D. (1982). Canopy temperature and crop water stress. In *Advances in irrigation* (Vol. 1, pp. 43–85). Elsevier. https://doi.org/10.1016/B978-0-12-024301-3.50009-5

Jackson, R. D., Idso, S. B., Reginato, R. J., & Pinter, P. J., Jr. (1981). Canopy temperature as a crop water stress indicator. *Water Resources Research*, *17*(4), 1133–1138. https://doi.org/10.1029/WR017i004p01133

Javadian, M., Scott, R. L., Woodgate, W., Richardson, A. D., Dannenberg, M. P., & Smith, W. K. (2024). Canopy temperature dynamics are closely aligned with ecosystem water availability across a water- to energy-limited gradient. *Agricultural and Forest Meteorology*, *357*, 110206. https://doi.org/10.1016/j.agrformet.2024.110206

Jeffers, D. L., & Shibles, R. M. (1969). Some effects of leaf area, solar radiation, air temperature, and variety on net photosynthesis in field-grown soybeans. *Crop Science*, *9*(6), 762–764. https://doi.org/10.2135/cropsci1969.0011183X000900060027x

Jones, H. G. (1999). Use of infrared thermometry for estimation of stomatal conductance as a possible aid to irrigation scheduling. *Agricultural and Forest Meteorology*, *95*(3), 139–149. https://doi.org/10.1016/S0168-1923(99)00030-1

Jones, H. G. (2004). Irrigation scheduling: Advantages and pitfalls of plant-based methods. *Journal of Experimental Botany*, *55*(407), 2427–2436. https://doi.org/10.1093/jxb/erh213

Jones, H. G. (2014). *Plants and microclimate: A quantitative approach to environmental plant physiology (3rd ed.)*. Cambridge University Press.

Jones, H. G., Serraj, R., Loveys, B. R., Xiong, L., Wheaton, A., & Price, A. H. (2009). Thermal infrared imaging of crop canopies for the remote diagnosis and quantification of plant responses to water stress in the field. *Functional Plant Biology*, *36*(11), 978–989. https://doi.org/10.1071/FP09123

Jones, H. G., Stoll, M., Santos, T., Sousa, C. de, Chaves, M. M., & Grant, O. M. (2002). Use of infrared thermography for monitoring stomatal closure in the field: Application to grapevine. *Journal of Experimental Botany*, *53*(378), 2249–2260. https://doi.org/10.1093/jxb/erf083

Karam, F., Masaad, R., Sfeir, T., Mounzer, O., & Rouphael, Y. (2005). Evapotranspiration and seed yield of field grown soybean under deficit irrigation conditions. *Agricultural Water Management*, *75*(3), 226–244. https://doi.org/10.1016/j.agwat.2004.12.015

Katimbo, A., Rudnick, D. R., DeJonge, K. C., Lo, T. H., Qiao, X., Franz, T. E., Nakabuye, H. N., & Duan, J. (2022). Crop water stress index computation approaches and their sensitivity to soil water dynamics. *Agricultural Water Management*, *266*, 107575. https://doi.org/10.1016/j.agwat.2022.107575

King, B. A., & Shellie, K. C. (2016). Evaluation of neural network modeling to predict non-water-stressed leaf temperature in wine grape for calculation of crop water stress index. *Agricultural Water Management*, *167*, 38–52. https://doi.org/10.1016/j.agwat.2015.12.009

Kirchsteiger, H., Pölzer, S., Johansson, R., Renard, E., & del Re, L. (2011). Direct continuous time system identification of MISO transfer function models applied to type 1 diabetes. *In 2011 50th IEEE Conference on Decision and Control and European Control Conference (pp. 5176–5181). IEEE*. https://doi.org/10.1109/CDC.2011.6161344

Klocke, N. L., Watts, D. G., Schneekloth, J. P., Davison, D. R., Todd, R. W., & Parkhurst, A. M. (1999). Nitrate leaching in irrigated corn and soybean in a semi-arid climate. *Transactions of the ASAE*, *42*(6), 1621–1630. https://doi.org/10.13031/2013.13328

Kruschke, J. K. (2014). Doing Bayesian data analysis: A tutorial with R, JAGS, and Stan (2nd ed.). Academic Press.

Kumari, A., Singh, D. K., Sarangi, A., Hasan, M., & Sehgal, V. K. (2024). Optimizing wheat supplementary irrigation: Integrating soil stress and crop water stress index for smart scheduling. *Agricultural Water Management*, *305*, 109104. https://doi.org/10.1016/j.agwat.2024.109104

Lee, S., Jo, C., Choi, M., Lee, J., Choi, N., & Na, C. (2025). Effect of plant topping on seasonal development, physiological changes, and grain yield of soybean. *Plants*, *14*(13), 2068. https://doi.org/10.3390/plants14132068

Liao, Q., Gu, S., Gao, S., Du, T., Kang, S., Tong, L., & Ding, R. (2024). Crop water stress index characterizes maize productivity under water and salt stress by using growth stage-specific non-water stress baselines. *Field Crops Research*, *317*, 109544. https://doi.org/10.1016/j.fcr.2024.109544

Lo, T. H., Rudnick, D. R., DeJonge, K. C., Bai, G., Nakabuye, H. N., Katimbo, A., Ge, Y., Franz, T. E., Qiao, X., & Heeren, D. M. (2020). Differences in soil water changes and canopy temperature under varying water × nitrogen sufficiency for maize. *Irrigation Science*, *38*(5), 519–534. https://doi.org/10.1007/s00271-020-00683-2

Locke, A. M., & Ort, D. R. (2015). Diurnal depression in leaf hydraulic conductance at ambient and elevated [CO2] reveals anisohydric water management in field-grown soybean and possible involvement of aquaporins. *Environmental and Experimental Botany*, *116*, 39–46. https://doi.org/10.1016/j.envexpbot.2015.03.006

Maes, W. H., & Steppe, K. (2012). Estimating evapotranspiration and drought stress with ground-based thermal remote sensing in agriculture: A review. *Journal of Experimental Botany*, *63*(13), 4671–4712. https://doi.org/10.1093/jxb/ers165

Mahan, J. R., Young, A. W., & Payton, P. (2015). Continuously monitored canopy temperature as a proxy for plant water status. *American Journal of Plant Sciences*, *6*(14), 2287–2302. https://doi.org/10.4236/ajps.2015.614232

Monje, O., & Bugbee, B. (2019). Radiometric method for determining canopy stomatal conductance in controlled environments. *Agronomy*, *9*(3), 114. https://doi.org/10.3390/agronomy9030114

Monteith, J. L., & Unsworth, M. H. (2013). Principles of environmental physics: Plants, animals, and the atmosphere (4th ed.). Academic Press.

Morales-Santos, A., & Nolz, R. (2023). Assessment of canopy temperature-based water stress indices for irrigated and rainfed soybeans under subhumid conditions. *Agricultural Water Management*, *279*, 108214. https://doi.org/10.1016/j.agwat.2023.108214

Nakabuye, H. N., Rudnick, D., DeJonge, K. C., Lo, T. H., Heeren, D., Qiao, X., Franz, T. E., Katimbo, A., & Duan, J. (2022). Real-time irrigation scheduling of maize using Degrees Above Non-Stressed (DANS) index in semi-arid environment. *Agricultural Water Management*, *274*, 107957. https://doi.org/10.1016/j.agwat.2022.107957

Nakabuye, H. N., Rudnick, D. R., DeJonge, K. C., Ascough, K., Liang, W., Lo, T. H., Franz, T. E., Qiao, X., Katimbo, A., & Duan, J. (2024). Weather data-centric prediction of maize non-stressed canopy temperature in semi-arid climates for irrigation management. *Irrigation Science*, *42*(2), 229–248. https://doi.org/10.1007/s00271-023-00863-w

Nielsen, D. C. (1990). Scheduling irrigations for soybeans with the crop water stress index (CWSI). *Field Crops Research*, *23*(2), 103–116. https://doi.org/10.1016/0378-4290(90)90106-L

Nielsen, D. C. (1994). Non water-stressed baselines for sunflowers. *Agricultural Water Management*, *26*(4), 265–276. https://doi.org/10.1016/0378-3774(94)90013-2

Norman, J. M., Kustas, W. P., & Humes, K. S. (1995). Source approach for estimating soil and vegetation energy fluxes in observations of directional radiometric surface temperature. *Agricultural and Forest Meteorology, 77*(3), 263–293. https://doi.org/10.1016/0168-1923(95)02265-Y

Orta, A. H., Erdem, Y., & Erdem, T. (2003). Crop water stress index for watermelon. *Scientia Horticulturae*, *98*(2), 121–130. https://doi.org/10.1016/S0304-4238(02)00215-7

Osroosh, Y., Peters, R. T., Campbell, C. S., & Zhang, Q. (2015). Automatic irrigation scheduling of apple trees using theoretical crop water stress index with an innovative dynamic threshold. *Computers and Electronics in Agriculture*, *118*, 193–203. https://doi.org/10.1016/j.compag.2015.09.006

Payero, J. O., Neale, C. M. U., & Wright, J. L. (2005a). Non-water-stressed baselines for calculating crop water stress index (CWSI) for alfalfa and tall fescue grass. *Transactions of the ASAE*, *48*(2), 653–661. https://doi.org/10.13031/2013.18329

Payero, J. O., Melvin, S. R., & Irmak, S. (2005b). Response of soybean to deficit irrigation in the semiarid environment of west-central Nebraska. *Transactions of the ASAE*, *48*(6), 2189–2203. https://doi.org/10.13031/2013.20105

Payero, J. O., Tarkalson, D. D., Irmak, S., Davison, D., & Petersen, J. L. (2009). Effect of timing of a deficit-irrigation allocation on corn evapotranspiration, yield, water use efficiency and dry mass. *Agricultural Water Management*, *96*(10), 1387–1397. https://doi.org/10.1016/j.agwat.2009.03.022

Peters, R. T., & Evett, S. R. (2004). Modeling diurnal canopy temperature dynamics using one-time-of-day measurements and a reference temperature curve. *Agronomy Journal*, *96*(6), 1553–1561. https://doi.org/10.2134/agronj2004.1553

R Core Team. (2025). *R: A language and environment for statistical computing*. R Foundation for Statistical Computing. https://www.R-project.org/

Sadler, E. J., Camp, C. R., Evans, D. E., & Millen, J. A. (2002). Corn canopy temperatures measured with a moving infrared thermometer array. Transactions of the ASAE, 45(3), 581–591. https://doi.org/10.13031/2013.8855

Sapkota, A., Haghverdi, A., & Merhaut, D. (2023). Effects of deficit irrigation on canopy temperature dynamics and physiology of landscape groundcovers. HortScience, 58(11), 1321–1331. https://doi.org/10.21273/HORTSCI17303-23

Sauer, T. J., Singer, J. W., Prueger, J. H., DeSutter, T. M., & Hatfield, J. L. (2007). Radiation balance and evaporation partitioning in a narrow-row soybean canopy. *Agricultural and Forest Meteorology*, *145*(3), 206–214. https://doi.org/10.1016/j.agrformet.2007.04.015

Saxton, K. E., & Rawls, W. J. (2006). Soil water characteristic estimates by texture and organic matter for hydrologic solutions. *Soil Science Society of America Journal, 70*(5), 1569–1578. https://doi.org/10.2136/sssaj2005.0117

Schymanski, S. J., Or, D., & Zwieniecki, M. (2013). Stomatal control and leaf thermal and hydraulic capacitances under rapid environmental fluctuations. *PLOS ONE*, *8*(1), e54231. https://doi.org/10.1371/journal.pone.0054231

Shae, J. B., Steele, D. D., & Gregor, B. L. (1999). Irrigation scheduling methods for potatoes in the northern Great Plains. *Transactions of the ASAE*, *42*(2), 351–360. https://doi.org/10.13031/2013.13366

Shapiro, C., Ferguson, R., Wortmann, C., Maharjan, B., & Krienke, B. (2019). Nutrient management suggestions for corn. *Department of Agronomy and Horticulture: Faculty Publications*. https://digitalcommons.unl.edu/agronomyfacpub/1449

Steele, D. D., Stegman, E. C., & Gregor, B. L. (1994). Field comparison of irrigation scheduling methods for corn. *Transactions of the ASAE*, *37*(4), 1197–1203. https://doi.org/10.13031/2013.28194

Taghvaeian, S., Chávez, J. L., Bausch, W. C., DeJonge, K. C., & Trout, T. J. (2014). Minimizing instrumentation requirement for estimating crop water stress index and transpiration of maize. *Irrigation Science*, *32*(1), 53–65. https://doi.org/10.1007/s00271-013-0415-z

Taghvaeian, S., Comas, L., DeJonge, K. C., & Trout, T. J. (2014). Conventional and simplified canopy temperature indices predict water stress in sunflower. *Agricultural Water Management*, *144*, 69–80. https://doi.org/10.1016/j.agwat.2014.06.003

Taylor, C. J., Pedregal, D. J., Young, P. C., & Tych, W. (2007). Environmental time series analysis and forecasting with the Captain toolbox. *Environmental Modelling & Software*, *22*(6), 797–814. https://doi.org/10.1016/j.envsoft.2006.03.002

Tekelioğlu, B., Büyüktaş, D., Baştuğ, R., Karaca, C., Aydınşakir, K., & Dinç, N. (2017). Use of crop water stress index for irrigation scheduling of soybean in Mediterranean conditions. *Journal of Experimental Agriculture International*, *18*(6). https://doi.org/10.9734/jeai/2017/37058

Testi, L., Goldhamer, D. A., Iniesta, F., & Salinas, M. (2008). Crop water stress index is a sensitive water stress indicator in pistachio trees. *Irrigation Science*, *26*(5), 395–405. https://doi.org/10.1007/s00271-008-0104-5

Tian, J., Wang, C., Chen, F., Qin, W., Yang, H., Zhao, S., Xia, J., Du, X., Zhu, Y., Wu, L., Cao, Y., Li, H., Zhuang, J., Chen, S., Zhang, H., Chen, Q., Zhang, M., Deng, X. W., Deng, D., … Tian, F. (2024). Maize smart-canopy architecture enhances yield at high densities. *Nature*, *632*(8025), 576–584. https://doi.org/10.1038/s41586-024-07669-6

Urban, J., Ingwers, M., McGuire, M. A., & Teskey, R. O. (2017). Stomatal conductance increases with rising temperature. *Plant Signaling & Behavior*, *12*(8), e1356534. https://doi.org/10.1080/15592324.2017.1356534

van Ravenzwaaij, D., Cassey, P., & Brown, S. D. (2018). A simple introduction to Markov Chain Monte–Carlo sampling. *Psychonomic Bulletin & Review*, *25*(1), 143–154. https://doi.org/10.3758/s13423-016-1015-8

Vialet-Chabrand, S., & Lawson, T. (2020). Thermography methods to assess stomatal behaviour in a dynamic environment. *Journal of Experimental Botany*, *71*(7), 2329–2338. https://doi.org/10.1093/jxb/erz573

Wanjura, D. F., Hatfield, J. L., & Upchurch, D. R. (1990). Crop water stress index relationships with crop productivity. *Irrigation Science*, *11*(2), 93–99. https://doi.org/10.1007/BF00188445

Wanjura, D. F., Upchurch, D. R., & Mahan, J. R. (2003). Crop water status control with temperature-time threshold irrigation (Paper No. 032136). 2003 ASAE Annual Meeting. https://doi.org/10.13031/2013.14012

Xie, S., Leib, B. G., Farhadi-Machekposhti, M., Grant, T. J., Adotey, N., & Butler, D. M. (2024). Soybean yield response to managed depletion irrigation regimes in a Mid-South silt loam soil. *Agricultural Water Management*, *292*, 108657. https://doi.org/10.1016/j.agwat.2023.108657

Yazar, A., Howell, T. A., Dusek, D. A., & Copeland, K. S. (1999). Evaluation of crop water stress index for LEPA irrigated corn. *Irrigation Science*, *18*(4), 171–180. https://doi.org/10.1007/s002710050059

Young, P. C. (2006). The data-based mechanistic approach to the modelling, forecasting and control of environmental systems. *Annual Reviews in Control*, *30*(2), 169–182. https://doi.org/10.1016/j.arcontrol.2006.05.002

Yuan, G., Luo, Y., Sun, X., & Tang, D. (2004). Evaluation of a crop water stress index for detecting water stress in winter wheat in the North China Plain. *Agricultural Water Management*, *64*(1), 29–40. https://doi.org/10.1016/S0378-3774(03)00193-8

Zhu, S., Han, D., Zhang, W., Yang, T., Yao, Z., Liu, T., & Sun, C. (2025). Development of maize canopy architecture indicators through UAV multi-source data. *Agronomy*, *15*(8), 1991. https://doi.org/10.3390/agronomy15081991

Appendix A - Growth-Stage-Specific Model Parameter Estimates and Advective Delays

Table A.1. Growth-stage-specific parameter estimates of the DBM model under cross-year calibration and validation for maize $\mathbf{T_{c,ns}}$. Values of **a**, **b**, and **c** are reported with approximate standard errors in parentheses.

Training year	Testing year	Stage	a	b	c
2018	2020	R4	0.0314 (0.3455)	0.2799 (0.3975)	0.3161 (0.2975)
2019	2020	V10	0.1022 (0.1910)	0.1763 (0.1280)	0.1771 (0.1816)
2019	2020	VT–R1	0.0542 (0.1556)	0.1210 (0.0991)	0.1368 (0.1123)
2019	2020	R2	0.1664 (0.2020)	0.1936 (0.1467)	0.3828 (0.2162)
2019	2020	R3	0.1261 (0.1321)	0.0243 (0.1288)	0.1379 (0.1384)
2020	2019	V8	1.1267 (0.2416)	0.1758 (0.1099)	1.2272 (0.2417)
2020	2019	V9	0.0461 (0.1045)	0.0308 (0.2328)	0.0789 (0.2393)
2020	2019	V10	0.0179 (0.2016)	0.0043 (0.0858)	0.0108 (0.1567)
2020	2019	R3	0.3562 (0.0850)	0.2255 (0.0641)	0.4040 (0.0983)
2020	2019	R4	0.1373 (0.4277)	0.6133 (0.4246)	0.6913 (0.6602)
2020	2018	R3	0.3688 (0.0802)	0.2681 (0.0646)	0.4486 (0.0975)
2019	2018	VT–R1	0.0542 (0.1556)	0.1210 (0.0991)	0.1368 (0.1123)
2019	2018	R2	0.1664 (0.2020)	0.1936 (0.1467)	0.3828 (0.2162)
2019	2018	R3	0.1261 (0.1321)	0.0243 (0.1288)	0.1379 (0.1384)

Table A.2. Stage-specific delay combinations selected for DBM model identification under different training and testing year combinations. The delays $\boldsymbol{\tau_a}$, $\boldsymbol{\tau_r}$, and $\boldsymbol{\tau_v}$ represent the selected integer-minute lags for air temperature, $\mathbf{R_s}$, and vapor pressure deficit, respectively.

Training year	Testing year	Stage	Air-temperature delay (min)	Radiation delay (min)	VPD delay (min)
2018	2020	R4	3	4	3
2019	2020	V10	2	1	1
2019	2020	VT–R1	0	0	0
2019	2020	R2	4	8	5
2019	2020	R3	0	0	1
2020	2019	V8	2	0	0
2020	2019	V9	7	8	5
2020	2019	V10	0	0	1
2020	2019	R3	1	0	2
2020	2019	R4	4	0	0
2020	2018	R3	0	0	0
2019	2018	VT–R1	0	0	0
2019	2018	R2	4	8	5
2019	2018	R3	0	0	1